Cu and Zn isotope fractionation during extreme chemical weathering

Susan H. Little[1,2]*, Sophie Munson[2], Julie Prytulak[3], Barry J. Coles[2], Samantha J. Hammond[4], Mike Widdowson[5]

1. Department of Earth Sciences, University College London, Gower Place, London, WC1E 6BS, UK.

*susan.little@ucl.ac.uk

2. Department of Earth Science and Engineering, Royal School of Mines, Imperial College London, London, SW7 2BP, UK.

3. Department of Earth Sciences, Durham University, Durham DH1 3LE, UK.

4. Department of Environment, Earth and Ecosystems, The Open University, Walton Hall, Milton Keynes, MK7 6AA, UK.

5. School of Environmental Sciences, Cohen Building, University of Hull, Hull, HU6 7RX, UK.

23 July 2019

For resubmission to *Geochimica et Cosmochimica Acta*

Abstract

Copper and Zn are trace metal micronutrients whose stable isotope systematics are receiving increasing attention as possible paleoenvironmental tracers. However, to realise this potential, their behaviour during chemical weathering must be better constrained. We present coupled Cu and Zn isotope data for a well-characterised Indian laterite weathering profile, which includes a full suite of samples from unaltered greywacke bedrock to indurated lateritic duricrust. This sample set provides an exceptional opportunity to interrogate Cu and Zn isotope compositions during an extreme example of chemical weathering. Despite their occurrence in different host phases within the parent greywacke, Cu and Zn isotopes behave coherently during weathering. We observe preferential loss of heavy isotopes at increasing degrees of alteration, with 0.6‰ total variability in δ^{66}Zn and 0.9‰ in δ^{65}Cu. Given the absence of evidence for CuS or ZnS phases in the parent lithology, we attribute the liberation of heavy isotopes to organic complexation in the aqueous phase and/or incorporation of light isotopes in secondary aluminous Fe-oxides. Strong enrichment of both metals is also associated with a peak in Mn at a previously identified paleo-water table horizon. This dataset confirms that weathering under oxygenated conditions releases isotopically heavy Cu, regardless of the host phase. Meanwhile, Zn isotopes are only fractionated to any significant extent at the most extreme degrees of chemical weathering reached during lateritization. We conclude that the isotopic composition of the weathering-derived input of Zn to rivers should be largely insensitive to climate change on geological timescales.

Keywords: Cu, Zn, Isotopes, Laterite, Weathering, Organic complexation, Fe oxides

1.0 Introduction

Variations in the stable isotope ratios of the bioessential transition metals Zn and Cu are increasingly being utilised as tracers of past Earth surface processes, particularly in the ocean (e.g., Kunzmann et al., 2013; Pons et al., 2013; Chi Fru et al., 2016; John et al., 2017; Isson et al., 2018). However, while isotopic shifts in sedimentary records of both Zn and Cu are undoubtedly present during periods of global change (e.g., Snowball Earth events in the Neoproterozoic), and often tantalisingly systematic (e.g., Kunzmann et al., 2013; John et al., 2017), their underlying controls remain difficult to elucidate.

Paleoceanographic interpretations of observed Zn and Cu isotope variations can be divided into one or more of three main causal categories. (1) Invoking a change in biological productivity (or other related process) in the ocean itself (Kunzmann et al., 2013; Isson et al., 2018). (2) Suggesting a change in the balance of the removal fluxes to different oceanic sinks, for example, due to a change in ocean redox state (Chi Fru et al., 2016; John et al., 2017). (3) Interpretations that require a change in the magnitude or isotopic composition of a *source* of the element to the ocean, for example, a change in the weathering-derived flux due to tectonic or climate change (Kunzmann et al., 2013; Pons et al., 2013; Chi Fru et al., 2016).

Weathering of the continents supplies solutes to rivers, which constitute a key input of Zn and Cu to the modern ocean (Little et al., 2014b). The Zn and Cu isotope composition of rivers will thus reflect that supplied by weathering, though biogeochemical processes in rivers may subsequently modify this primary signature (e.g., Borrok et al., 2008; Coutaud et al., 2014; Szynkiewicz and Borrok, 2016; Coutaud et al., 2018). The aim of this study is to investigate Zn and Cu isotope fractionation during extreme chemical weathering. This approach provides an end-member constraint on the degree of isotope fractionation possible in the weathering environment. It is a starting point from which to evaluate the leverage of chemical weathering in modifying the isotopic composition of rivers through time, and hence its possible influence on the wider marine inventory.

A study of the dissolved phase in rivers found a discharge-weighted Zn isotope composition unfractionated from continental rocks (Little et al., 2014b). The absence of systematic Zn isotope fractionation in rivers implies little or no Zn isotope fractionation during weathering, a hypothesis partially supported by studies of Zn isotopes in soils (Bigalke et al., 2010a; Vance et al., 2016; Opfergelt et al., 2017; Suhr et al., 2018). However, studies carried out in extreme, (sub-) tropical weathering regimes have observed preferential release of heavy Zn isotopes (Viers et al., 2007; Lv et al., 2016; Guinoiseau et al., 2017; Suhr et al., 2018). This observation has been explained by various processes, including release of isotopically heavy Zn during oxidative weathering of sulphides (Fernandez and Borrok, 2009; Lv et al., 2016); organic complexation of the heavy isotope in the dissolved pool (Guinoiseau et al., 2017); incorporation or adsorption of isotopically light Zn in/on clays (Viers et al., 2007; Guinoiseau et al., 2017) or Fe oxides (Viers et al., 2007; Suhr et al., 2018); or release of isotopically light Zn from refractory mineral phases and subsequent re-precipitation with Fe oxide phases (Suhr et al., 2018).

In contrast to Zn, Cu in the riverine dissolved pool is isotopically heavy relative to rocks (Vance et al., 2008); this behaviour is similar to observations for Mo (Archer and Vance, 2008; Neubert et al., 2011), Li (Huh et al., 1998), Ni (Cameron and Vance, 2014), and Cr isotopes (Frei et al., 2014). Accordingly, there are two proposed explanations for the heavy Cu isotope composition in rivers: (1) An equilibrium isotope fractionation in rivers (Vance et al., 2008) and/or in soils (Vance et al., 2016) between an isotopically heavy, organic ligand bound, dissolved pool and an isotopically light pool sorbed to particulates; (2) Redox-driven release of isotopically heavy Cu during oxidative weathering of sulphides in black shales or supergene systems (Mathur et al., 2005; Mathur et al., 2012; Mathur and Fantle, 2015; Lv et al., 2016).

The present study investigates the Zn and Cu isotope systematics of a well-characterised Indian lateritic weathering profile. The term laterite is not always used ubiquitously or consistently. We follow the definition in the widely cited *Encyclopaedia of Geomorphology* (Goudie, 2004; Widdowson, 2004), which states that: ‘Laterite is an iron-rich, sub-aerial, weathering product, commonly believed to

evolve as a result of intense, *in situ* substrate alteration under tropical or sub-tropical climatic conditions.' A lateritic weathering profile therefore constitutes a chemical residuum resulting from the relative enrichment of relatively immobile elements (notably Fe and Al), as described initially by Newbold (1844), and more recently by many other authorities (e.g., McFarlane, 1976; McFarlane, 1983; Schellman, 1983; Aleva, 1984; Widdowson, 2004, 2007; Babechuk et al., 2014). This definition emphasises the relative enrichment of Fe (and Al) through desilication processes involved in the development of a laterite profile; this enrichment/depletion may be modified through hydromorphism associated with oscillating redox conditions in the developing weathering profile and typically driven by pluvial seasonality and associated water-table recharge.

Laterites typically form on parent lithologies with inherently high iron contents (such as mafic and ultramafic igneous rocks and chemically immature sediments) and on stable continental landmasses subject to high mean annual temperatures, high humidity and seasonal, high annual rainfall (Widdowson, 2007). These climatic conditions promote intense *in situ* chemical weathering and mineral alteration, making laterites an ideal natural laboratory to study the weathering process *in extremis*. Today, laterites and associated weathering products account for approximately 30% of Earth surface cover, and almost 50% of continental drainage flows over these terrains (Tardy, 1997).

To date, two studies have reported Zn isotope data from lateritic weathering profiles, one developed on granodiorite in Cameroon (Viers et al., 2007) and the other for the Bidar laterite developed on Deccan basalt in central India (Suhr et al., 2018). Both studies observe preferential retention of light Zn isotopes in the laterite residues. To the best of our knowledge, no Cu isotope data for laterites has yet been reported.

2.0 Geological setting and background

2.1 Geological setting

The coastal lowlands of western peninsular India between ~8° and ~19°N comprise dissected, laterite-capped 'tablelands' with maximum altitudes of ~150–200m in the east systematically descending to less than 50–100m at the coastline (Widdowson, 2009). These tablelands are remnants of a once extensive laterite belt that extended along the length of western peninsular India (Widdowson, 2009), developed upon a variety of lithologies. This belt provides evidence of an important phase of Cenozoic lateritization that affected western India during the latest Eocene to the Miocene (Schmidt et al., 1983; Bonnet et al., 2014), when climatic conditions were optimal for deep weathering (Tardy et al., 1991).

The site of the investigated profile lies in the small coastal state of Goa. Metamorphic rocks of varying grade and composition dominate the geology of Goa (Pascoe, 1950) and include weakly metamorphosed Dharwar sediments of the Dharwar craton, including abundant Late Archaean greywackes (Argast and Donnelly, 1986; Devaraju et al., 2010; Dessai, 2011). The samples in this study (hereafter referred to as 'SQ') are from a quarried laterite profile developed upon meta-greywackes of the Sanvordem Fm (of the Proterozoic age Dharwar Supergroup; > 2.5 Ga) at Merces village, near Panjim Goa (15°28'44"N, 73°52'35"E; Fig. 1).

The parent greywacke consists of a detrital assemblage of quartz, feldspar and volcanic rock fragments (Srinivasan et al., 1989) and geochemical analysis suggests that the bulk sediment was derived from submarine weathering of a felsic volcanic source (Devaraju et al., 2010). Sparse biotite has developed in response to low-grade thermal metamorphism of unknown age. The SQ laterite profile itself is of probable Oligocene-Miocene age (c. 35 – 20 Ma; Schmidt et al., 1983; Bonnet et al., 2014), and developed upon the low-lying coastal (Konkan) plain, subsequent to erosion (i.e. removal of c.1 – 1.5km thickness) across the Indian continental margin (Widdowson, 1997; Widdowson and Gunnell, 1999).

2.2 Sample description

The lithology and mineralogy of the 34 m thick laterite profile has previously been reported in Wimpenny et al. (2007) as the SQ samples series, and comprehensively in Hibbert (2017) as an independent MQ sample series. A schematic diagram of the SQ

profile is shown in Figure 2 (mineralogy and major element data from Wimpenny et al., 2007). Samples SQ2 – SQ14 were sampled from increasingly shallow depths and represent a greywacke parent that has undergone increasing degrees of alteration (Table S1; Figs. 2, 3). Sample SQ1 was taken from a small mafic dyke, which cuts unaltered greywacke near the base of the profile. All samples have previously been analyzed for major element (Table S2) and high-precision trace element concentrations (Table S3) (Howarth et al., 2018; Wimpenny et al., 2007).

Deep lateritic weathering profiles such as the one described here have considerable antiquity and affect the substratum far below that of modern pedogenetic processes. The degree of alteration progresses upward from unaltered 'parent' material, through saprock to saprolite, through a 'mottled zone', and ultimately to the topmost Fe-rich laterite duricrust (i.e. 'carapace' and then indurated 'cuirasse' in the francophone terminology).

Saprock (from the Greek '*sapros*' meaning 'rotten') is the first stage of weathering: It consists of partially weathered minerals and as yet unweathered minerals (e.g., feldspars have begun to alter to clay minerals and/or olivine to iddingsite). Saprock maintains all the fabrics and features of the fresh rock, and is distinguished from the more advanced stage of saprolite by retaining much of its original physical strength, and some primary mineralogy. Saprolite is more altered than saprock but, like saprock, there has been little or no change in bulk volume, and the distribution of resistant minerals remain more or less in position as they occurred in the parent. Weatherable minerals in saprolite are typically wholly pseudomorphed by clays and/or oxides and oxyhydroxides, whilst the original rock fabric remains largely preserved (Taylor and Eggleton, 2001). In the zone of alternating reduction and oxidation due to repeated wetting and drying, segregation of iron occurs, forming 'mottles'. The uppermost laterite duricrust hardens irreversibly due to complete drying and oxic conditions, and consists predominantly of crystallised Fe and Al oxide and oxyhydroxides.

The SQ profile can be divided into four zones of alteration (Figs. 2, 3), as defined by Wimpenney et al. (2007):

Zone I, at 34 – 15m depth (samples SQ2 – SQ6), exhibits no alteration (parent rock) or low degrees of alteration while retaining the primary texture and fabric of the bedrock (saprock);
Zone II, at 15 – 8.5m depth (samples SQ7 – SQ9), consists of altered saprolite in which most weatherable primary minerals are destroyed, then passing into a 'mottled' region, in which secondary minerals and Fe-Al-rich accretions (i.e. mottles) form;
Zone III, at 8.5 – 7m depth (samples SQ10 and SQ11), is a narrow zone thought to be influenced by a paleo-water table (Wimpenny et al., 2007);
Zone IV, at 7m – surface (samples SQ12 – SQ14), is the Fe-rich cap in which secondary minerals are removed and the Fe-Al-rich accretions fuse to form a resistant, indurated laterite duricrust.
The 'line of seepage', at ~15m depth, divides little altered greywacke (zone I) from the zones of increasing alteration above, and is so-called because it marks a significant increase in porosity and permeability (Wimpenny et al., 2007).

The mineralogical changes that occur upwards in the profile (Table S1, Fig. 3) are reflected in variations in major element concentrations (Table S2, Fig. 2), characterized by a general decrease in Si and concomitant enrichment in Fe and Al (Wimpenny et al., 2007; Widdowson, 2009). In the low alteration zone I, the range of major element concentration variations are somewhat limited (Table S2, Fig. 2) and are likely related to lithological heterogeneity in the parent greywacke (Widdowson, 2009). Above the line of seepage, in zones II and IV, there is an increasing degree of depletion of more mobile elements (e.g., Si, Mg, Ca, Na, K), due to the formation and then breakdown and removal of secondary clay minerals, generating the observed enrichment of less mobile elements (e.g., Fe, Al and Ti) in the residue (Widdowson, 2009). Notably, this broad pattern is interrupted at ~7 – 8.5m depth (zone III; samples SQ10 and 11) by significantly elevated concentrations of Fe and Mn and depletion of Al; previously interpreted as the depth of a paleo-water table (Fig. 2; Wimpenny et al., 2007).

Trace element concentrations exhibit similar coherent trends as the rock becomes increasingly altered in zones II-IV (Wimpenny et al., 2007; Howarth et al., 2018). Some fluid-mobile elements (e.g., Li, Rb, Ba, Cu, Zn) show a general decrease in concentration towards the surface but a pronounced peak at the paleo-water table (Fig.

S1A). Other fluid mobile elements, particularly the REE and PGEs, show enrichment at the paleo-water table and in zone IV (Fig. S1B), this is attributed to mobilization in low pH, high Eh conditions below, followed by scavenging from solution and incorporation in the oxide phases that precipitate above (Wimpenny et al., 2007). By contrast, relatively immobile elements (e.g., Zr, Ti, Nb) display a general increase in concentration towards the surface and a pronounced concentration decrease at the paleo-water table (Fig. S1C).

3.0 Analytical Methods

3.1 Sulphur analyses

Sulphur concentrations were measured on an aliquot of solution previously digested for high precision trace element analysis (see Howarth et al., 2018, for details on digestion techniques). Analyses were conducted on an Agilent triple quadrupole ICP-MS (ICP-QQQ) at the Open University. For conventional ICP-MS systems measuring sulphur concentrations has been challenging, owing to the high background contribution (from O_2). The ICP-QQQ has an octopole reaction system (ORS) that separates two quadrupole mass filters, allowing for targeted interference removal. For S we use O_2 as the reactive gas, forming SO^+ as the product in the ORS, and measure the mass shifted oxide ion (i.e. at mass 50 for ^{34}S). This effectively reduces the background from ~1.1 x 10^4 cps to ~2 x 10^2 cps. Detection limits are 0.2 ng/g in the solutions (equivalent to 0.2 µg/g in the rock – samples are diluted 1000 fold prior to analysis). Analyses were standardised against a suite of five reference materials (BIR-1, W-2, BHVO-2, AGV-1, BE-N) measured at the start of each analytical session. An internal standard solution was also bled in online throughout the analytical session, and used to monitor and correct for instrument drift. In addition, a monitor block, consisting of BHVO-2 (digested at Imperial College with the unknowns and not used in the calibration) BE-N and 2% HNO_3 was run every 4 – 5 unknowns to further monitor drift, and to monitor precision and accuracy of measurements.

The reference materials used in the calibration have only information values listed in the GEOREM database (and where uncertainties are quoted these are also large, e.g BHVO-2 = 164 ± 25 µg/g). However, for the majority of materials we find that using these information values yields a calibration line with an R^2 value of 0.9995. We also find that rock reference materials behave very similarly to the samples during ionisation in the plasma, and therefore find this a more robust method of calibrating rather than having to apply an ionisation correction to a suite of synthetic calibration materials. The one outlier from our calibration line is BIR-1. Further investigation by standard addition methods indicate that the concentration of S is 4.5 µg/g in three further BIR-1 digests from our powder aliquot (rather than 70 µg/g as quoted from GEOREM) and, when this is taken into account, the BIR-1 measurements again sit on the calibration line as described above, and do not alter the R^2 value of the line. We find that our repeat measurements of the BHVO-2 standard digested at Imperial College show both a precision and accuracy of <4 % (RSD) compared to the information values given. Whilst some caution must be exercised in using these information values, we remain confident in the relative concentration variations within our sample suite.

3.2 Zn and Cu isotope analyses

All isotopic analytical work was carried out in the MAGIC clean laboratories at Imperial College London using deionized 18.2 MΩ water (MQ), Teflon-distilled acids (HF, HNO_3 and HCl), Suprapur H_2O_2, and acid-cleaned Savillex PFA labware. 20 mg of each sample was digested in a ~3:1 HF:HNO_3 mix at 140°C for ~48 hours. After drying down to a gel-like consistency, samples were treated three times with concentrated HNO_3 to drive off fluoride salts. Previously published high precision trace element data for the same sample powders (Howarth et al., 2018) were used to estimate the appropriate volume of a ^{64}Zn-^{67}Zn double spike required to obtain a Zn spike:sample ratio of approximately 1.2 (Arnold et al., 2010; Bridgestock et al., 2014). After spike equilibration, conversion to chloride, and re-dissolution in 7M HCl + trace H_2O_2, Cu and Zn fractions were purified from the same digest solutions via anion exchange using AG MP-1M resin (BioRad), as detailed previously (Maréchal et al., 1999; Archer and Vance, 2004; Little et al., 2014b). Due to the highly refractory nature of the samples (i.e. high concentrations of potentially interfering elements such

as Ti and Fe), three column passes were performed for both the Cu and Zn fractions. The final Zn column was smaller in volume, following Bridgestock et al. (2014).

Prior to analysis, purified Cu fractions were refluxed overnight in HNO_3 + H_2O_2 and purified Zn fractions were treated twice with ~100 µL HNO_3, with the intention of eliminating residual resin-derived organics, before final re-dissolution in 1 mL 2% HNO_3. Aliquots of these solutions were diluted to final concentrations of ~100ppb total Zn (i.e. spike + sample Zn) and ~100ppb Cu for analysis. For both Cu and Zn, the USGS rock standards BHVO-2, BIR-1A, BCR-2 and Nod-P1 were processed using the same procedures and analysed to assess accuracy. Table 3 compares our data with previously published $\delta^{66}Zn$ and $\delta^{65}Cu$ values.

Zinc isotope analyses followed protocols described previously (Arnold et al., 2010; Bridgestock et al., 2014). Briefly, measurements were made on a Nu Plasma HR MC-ICP-MS equipped with an ARIDUS II (CETAC Technologies) desolvating system and nominal 100 µL/min MicroMist glass nebulizer, in low resolution mode. Instrumental sensitivities were >100 V/ppm Zn. Data collection (3 × 20 5s integrations) was preceded by an analysis (15 5s integrations) of the 2% HNO_3 used to dilute solutions, with subtraction of these "on-peak zeroes" from sample signals. Instrumental mass bias was corrected via the double spike technique described in Arnold et al. (2010) and Bridgestock et al., (2014). Data reduction was carried out offline following Siebert et al. (2001), with corrections for spectral interferences from ^{64}Ni (via monitoring ^{62}Ni) and Ba^{2+} ions (via monitoring at mass 68.5). Interference corrections were negligible, however, with $^{64}Ni^{+}/^{64}Zn^{+}$ and $^{134}Ba^{2+}/^{67}Zn^{+}$ levels at less than 1 x 10^{-5} in all cases. The Zn isotope ratios of samples were determined relative to matching (spike:natural Zn ratio and total Zn) standard solutions of IRMM-3702:

Eqn. 1: $\delta^{66}Zn = [(R_{Sample}/R_{Standard}) - 1] \times 1{,}000$

Final values are reported normalised to JMC Lyon by applying a correction of +0.30‰, as recommended in the recent review by Moynier et al. (2017). Over the course of this study the long-term reproducibility of a secondary standard, the in-house 'London Zn', was $\delta^{66}Zn_{JMC\text{-}Lyon}$ = +0.08 ± 0.07‰ (n = 99, 2 SD), compared with +0.08 ± 0.04‰ (n = 10, 2 SD) reported by Arnold et al. (2010) and +0.12 ± 0.04‰ (n = 6, 2 SD) by Larner and Rehkämper (2012). Total procedural blanks for

Zn were 3.6 ± 2.6 ng (n = 8, 1 SD), less than 1% of the Zn content of the smallest sample. Yields were 104 ± 10% (1 SD).

Copper isotope analyses employed a Nu Plasma II HR MC-ICP-MS at Imperial College London. Measurements were made in low resolution mode, with introduction via a Peltier cooled (to 5°C) glass spray chamber coupled to a ~100 µL/min glass nebulizer. Instrumental mass bias was corrected via doping with Ni following e.g., Ehrlich et al. (2004) and Larner et al., (2011). Nickel was chosen ahead of Zn for this study because it has a first ionization potential (7.64 eV) close to that of Cu (7.72 eV) and it is less sensitive to contamination. All samples and standards were doped to achieve a Ni:Cu ratio of 3 to 4, matched to within ± 5%. Tests at variable Ni/Cu ratios (2 to 5) suggested that neither accuracy nor precision is sensitive to the selected Ni:Cu ratio. Analyses were carried out in static mode using Faraday cups to monitor masses 60, 61, 62 (for Ni), and 63, 65 (for Cu).

Data collection consisted of 60 x 5s integrations preceded by an analysis (15 x 5s integrations) of the 2% HNO_3 solution, with the latter subtracted from sample signals. Sensitivity for Cu was typically ~25 V/ppm. The exponential law was used to mass bias correct measured $^{65}Cu/^{63}Cu$ ratios relative to $^{62}Ni/^{60}Ni$. $\delta^{65}Cu$ values were then calculated as the deviation of the mass bias corrected $^{65}Cu/^{63}Cu$ ratio of the sample relative to two bracketing standards (ERM-AE633):

Eqn. 2: $\delta^{65}Cu = [(R_{Sample}/R_{ERM\text{-}AE633}) - 1] \times 1{,}000$

This combination of external element doping and standard-sample bracketing has previously been described for e.g., Tl with Pb (Nielsen et al., 2004) and for Cu with Ni (Larner et al., 2011).

Finally, the minor reported offset of -0.01‰ between AE633 and the international standard NIST SRM 976 was applied, such that data are reported normalised to SRM 976 (Moeller et al., 2012). The long-term reproducibility of a secondary Romil Cu solution standard was $\delta^{65}Cu_{SRM\text{-}976} = +0.23 \pm 0.07$‰ (n = 22, 2 SD), comparable to the +0.20 ± 0.08‰ (n = 5, 2 SD) reported by Larner et al. (2011). Total procedural blanks for Cu were 4.9 ± 1.7 ng (n = 4, 1 SD), less than 1% of the Cu content of the smallest sample. Yields, estimated by comparison of Cu concentration data from the

OU (Howarth et al., 2018) with concentrations from the isotopic analysis (obtained by a less precise beam matching approach), were 93 ± 9% (1 SD). Complete yields are essential for Cu isotope analyses due to the potential for isotopic fractionation during anion exchange (Maréchal and Albarède, 2002); no relationship is observed between sample isotopic composition and calculated yield, corroborating the accuracy of the Cu isotope data presented here.

3.3 Calculating CIA, IOL and τ –values

Two useful measures of the degree of weathering are presented. First, the Chemical Index of Alteration (CIA) is calculated following Nesbitt and Young (1982). CIA utilises the molar mass of key indicator elements:

Eqn. 3: $CIA = [Al_2O_3/(Al_2O_3 + CaO^* + Na_2O + K_2O] \times 100$

[Where each compound is expressed as its molar mass]

CaO* is the amount of CaO incorporated in the silicate fraction of the rock. Since CaO contents of the SQ samples are low (<1 wt%), and because inherent carbonate phases were absent, no correction for the sample carbonate content was deemed necessary. CIA effectively tracks feldspar dissolution and the concomitant release of Ca, Na, and K relative to Al, since the latter is typically retained within resulting clays. Most igneous rocks of varying composition will plot between a CIA value of 35 and 55, with mafic rocks occupying the lower values. Unaltered granites and granodiorites, which may be representative of the greywacke protolith of the SQ profile, have CIA values of between 45 and 55. By comparison, sample SQ2 has a CIA value of 57 (Table 2; Fig. 2).

Second, Babechuk et al., (2014) suggest an alternative means to chemically characterise the stages of extreme weathering at which the CIA becomes ineffective, the Index of Lateritisation (IOL; Table 2, Fig. 2):

Eqn. 4: $IOL = 100 \times [(Al_2O_3 + Fe_2O_{3(T)}) / (SiO_2 + Al_2O_3 + Fe_2O_{3(T)})]$

Enrichment or depletion of an element can be quantified by comparison to an immobile reference element. For this purpose, we calculate the tau (τ) parameter (after Chadwick et al., 1990):

366 Eqn. 5: $\tau_{i/j} = \left[\frac{(\frac{C_i}{C_j})_h}{(\frac{C_i}{C_j})_p}\right] - 1$

367 Where C is the measured concentration, i is the element of interest (e.g.. Zn, Cu), j is
368 an immobile reference element (Nb, Ti or Zr), h is the weathering product, and p the
369 unaltered parent lithology. A value greater than zero indicates net gain of an element
370 relative to the parent material at that horizon within the weathering profile, while a
371 value less than zero indicates loss.
372
373 Two approaches were used to investigate uncertainty in τ –values. First, we compared
374 τ-values calculated assuming p is represented by the deepest sample in the section
375 (SQ2) with those calculated by taking an average of all samples from the little altered
376 zone I (SQ2 – SQ6). Second, Babechuk et al. (2014) advocate the use of Nb as the
377 most appropriate immobile reference element (j) for lateritic sample suites. In
378 addition, and for comparison, we compare τ-values calculated using Nb with those
379 determined using immobile elements Ti and Zr. Importantly, we find no significant
380 difference in absolute values or patterns of elemental enrichment or loss independent
381 of the choice of p or j (Fig. S2, Fig. 4).
382
383
384 # 4.0 Results
385
386 ## 4.1 Zn and Cu concentrations and enrichment-depletion patterns (τ-values)
387
388 Copper concentrations exhibit limited absolute variability up-section (31 – 66 µg/g)
389 compared to larger variations in Zn (21 – 146 µg/g) (Table 2, Fig. 4A). Both Cu and
390 Zn concentrations decrease in stepwise fashion across the line of seepage, which
391 represents the transition from zone I to zone II at ~15m depth (Fig. 4A). Elevated
392 concentrations of both elements are observed at 7.5m (zone III, sample SQ11), the
393 uppermost depth of the paleo-water table (Wimpenny et al., 2007). The surface-most
394 sample (SQ14) has distinctly higher Cu and Zn concentrations compared to the other
395 two samples beneath; together these three samples make up the Fe-rich duricrust
396 (zone IV).

Both τ_{Zn} and τ_{Cu} become increasingly negative up section, with up to ~90% Zn and ~70% Cu depletion relative to the protolith composition (Fig. 4B). The pattern of enrichment and depletion of both elements above the line of seepage (at ~15m) is similar, with marked depletion immediately above this transition, interrupted by a sharp peak of enrichment at the paleo-water table, followed by more moderate enrichment in the uppermost sampling horizon (SQ14, particularly evident for τ_{Cu}). τ_{Zn} exhibits a very strong correlation with τ_{Li} throughout the laterite profile, while τ_{Cu} is decoupled from both τ_{Li} and τ_{Zn} in zone I, at 15m and below (Fig. 4B).

4.2 Zn and Cu isotope systematics

The unaltered greywacke protolith, represented by sample SQ2 at 34 m, has a Zn isotope composition of +0.50 ± 0.04‰ (n = 2, 2SD). This value is isotopically heavy compared to typical lithogenic Zn in clastic sediments, at +0.28 ± 0.13‰ (n = 105, Moynier et al., 2017). For Cu, sample SQ2 has a Cu isotope value of +0.03 ± 0.05‰ (n = 2, 2SD), which is within the typical range for Cu in clastic sediments at +0.08 ± 0.20‰ (n = 42, Moynier et al., 2017).

In the low alteration zone I, below the line of seepage (samples SQ2 to SQ6, 34 to 15 m), Zn isotope ratios do not vary outside of analytical uncertainty (δ^{66}Zn = +0.47 ± 0.09‰, n = 5, 2SD). Copper isotope ratios show a resolvable shift from ~0‰ at the base of the profile to lower values at 22.5m (SQ5, -0.28‰) and 15m (SQ6, -0.23‰) (Fig. 5A).

Above the line of seepage in zones II–IV (15 m – surface), samples SQ7 to SQ14 show considerably more marked, correlated shifts in Zn and Cu isotope compositions. This is manifest as a general trend towards lower δ^{66}Zn and δ^{65}Cu upwards in the weathering profile (Fig. 5). Again, the paleo-water table interrupts this trend in δ^{65}Cu, with a marked offset towards a higher Cu isotope ratio (at -0.30‰) compared to the samples directly above and below (at -0.86‰ and -0.65‰ respectively). The surface-most sample (SQ14) is isotopically lightest for both Cu (at -0.87‰) and Zn (at -0.02‰). In summary, the total variability up section in δ^{65}Cu is 0.91‰, which is greater than that observed for δ^{66}Zn, at 0.55‰.

5.0 Discussion

5.1 Zone I: Host phases and lithological heterogeneity in the low alteration zone (parent – saprock)

Wimpenny et al. (2007) described the mineralogical variations through the SQ sequence, which we briefly recount here. The deepest greywacke sample (SQ2, 34 m) comprises 75% quartz, 15% biotite, 5% plagioclase, 2% opaques and 3% other minerals (Wimpenny et al., 2007). Up-section in zone I (SQ2 – SQ6 at 34 – 15m), lithological variability is observed (Fig. 3). For example, biotite contents vary between 8 and 20%, plagioclase from 2 – 8% and quartz from 74 – 80%. Secondary clay minerals (e.g., kaolinite) are not observed in zone I (Fig. 3), confirming the limited extent of chemical weathering at these depths. CIA values are consistent with this inference, and remain essentially unchanged between the base of the profile (CIA = 57 at 34m) to the top of zone I (CIA = 59 at 15m; Fig. 2)

Lithological variability is reflected in the major and trace element geochemistry of the zone I samples. Al_2O_3, Fe_2O_3, MgO, Li and many other trace element concentrations positively co-vary with biotite crystal content in this zone (Table S1, S3; Fig. S3). SiO_2 concentrations show the opposite trend (Fig. S4). These observations are consistent with known minor lateral variation in the quarry (Hibbert, 2017) and are likely linked to a grain size control on mineralogy and geochemistry, as previously recognised in sedimentary settings (e.g., Vdović et al., 1991; Roser et al., 1996; Lupker et al., 2011). Accordingly, Al_2O_3 and SiO_2 contents generally correlate and anti-correlate with grain size respectively, due to the predominance of aluminium-rich phyllosilicates (like biotite) in the fine grain size fraction.

Zinc concentrations in zone I samples correlate with biotite content (Fig. S3B), as well as with several trace elements and major oxides that are commonly hosted in biotite, including Li, Co, Rb, Cs and Tl, MnO, MgO and K_2O (Fig. 6A, C, data from Howarth et al., 2018). Potassium and Mg are both key structural components in

biotite ($K_2(Mg,Fe^{2+})_{6-4}(Fe^{3+},Al,Ti)_{0-2}[Si_{6-5}Al_{2-3}O_{20}](OH,F)_4$) (Deer et al., 1992). Manganese and Li are commonly substituted into biotite octahedral sites, and Cs, Rb and Tl commonly replace K in interlayer sites (Deer et al., 1992; Gomez-Gonzalez et al., 2015). These observations suggest that the Zn present in the parent greywacke is principally hosted within biotite.

Both Zn and Cu are chalcophile and, if sulphide phases were present, would be expected to strongly partition into these phases. However, measured S concentrations in the SQ profile are low (<0.1 wt%, Fig. 6, Table 2) and, while there is a positive correlation between Zn and S concentrations in zone I samples (Fig. 6G), a negative correlation is observed between Cu and S concentrations (Fig. 6H). This observation appears to rule out the presence of CuS phases in the parent lithology. Furthermore, Banks (1973) reports 116 – 316 μg/g S in biotite, suggesting that biotite-hosted S provides a satisfactory explanation for the correlation of Zn with S (Fig. 6G).

In contrast to Zn, Cu shows negative correlations with almost all elements in zone I except SiO_2 and Na_2O (Fig. 6). As discussed, higher SiO_2/Al_2O_3 ratios likely reflect a coarser grain size. Higher Na_2O contents in sandstone versus siltstone have been hypothesised to reflect a greater abundance of detrital plagioclase (Roser et al., 1996), but no correlation is observed between Na_2O and plagioclase abundance in the SQ sample set. Plagioclase contains only scarce quantities of trace elements (Deer et al., 1992), in any case, making this an unlikely Cu host. We conclude that identification of the Cu host phase(s) requires detailed micro-analytical work that is beyond the scope of this study. Nevertheless, we suggest that Cu is present in one or more detrital phase(s), the abundance of which is greater in the coarser grained beds of the greywacke.

To summarise, the τ_{Zn} and τ_{Cu} values in zone I samples similarly reflect primary lithological heterogeneity of the greywacke, rather than recording any elemental mass transfer. Thus, in order to take account of this heterogeneity in calculating τ-values, we use an average of all samples in zone I as the best estimate of the parent material ('p' in Eqn. 5). This approach, rather than simply selecting the least altered sample SQ2, leads to a greater coherence of the calculated τ-profiles for different elements

(e.g., Zn cf. Li) and for the same element using different immobile reference elements (e.g., Ti, Zr, 'j' in Eqn. 5; Fig. S2).

Isotopically, the greywacke $\delta^{65}Cu$ lies within the range of typical clastic sediments, at about 0‰ (Moynier et al., 2017). For $\delta^{66}Zn$, however, it is isotopically heavy (e.g., sample SQ2 at +0.50‰) relative to lithogenic Zn (at about +0.3‰; Moynier et al., 2017). Similarly isotopically heavy Zn has been observed in biotite-granites from the Kaapvaal craton, South Africa (Doucet et al., 2018), from Taiwanese andesite, sandstones and suspended river sediment (Bentahila et al., 2008), and in granitoids from the Nyong Basin, Cameroon (Viers et al., 2007) and the Lachlan Fold Belt, Australia and Black Hills, South Dakota, USA (Telus et al., 2012).

At 22.5m (sample SQ5), a small shift (of about –0.3‰) towards a lower $\delta^{65}Cu$ value is observed (Fig. 5). This shift may either be a primary lithological signature, or indicate the earliest detectable onset of oxic chemical weathering. Sample SQ5 has the highest phyllosilicate abundance (sum of biotite, muscovite and chlorite, 23%; Table S1, Fig. 3) and a slightly elevated CIA value (of 63; Table 2, Fig. 2) compared to the other samples in zone I (at 12–15% and 57–59 respectively). The high abundance of easily weatherable, fine fraction phyllosilicates increases the susceptibility of this sample to alteration (Goldich, 1938).

Overall, elemental variations in the low alteration zone I can primarily be explained by lithological heterogeneity in the parent greywacke. Copper and Zn isotopes in this zone exhibit small shifts, either reflecting this lithological heterogeneity and/or early stage chemical alteration. A greater spatial resolution of sampling in the quarry would improve constraints on the importance of lateral variability and lithological heterogeneity.

5.2 Zones II and IV: the Mottled and Laterite Zones

Above the line of seepage, the mottled and laterite zones (II and IV) are characterised by depletion of Cu and Zn (observed in negative τ_{Cu} and τ_{Zn}) and isotopically light $\delta^{65}Cu$ and $\delta^{66}Zn$ values (Figs. 4, 5). This pattern could reflect either (i) preferential

release of heavy isotopes during mobilization from (i.e. dissolution of) the host phase, or (ii) isotope fractionation in the aqueous phase and/or during precipitation of secondary Fe oxide phases.

5.2.1 Isotope fractionation during host mineral dissolution

Mineral dissolution may be accompanied by isotope fractionation. For example, isotopically light Zn and Cu in weathered black shales from China and the USA have been interpreted to result from preferential release of heavy Cu and Zn isotopes during oxidative weathering of sulphide minerals (Mathur et al., 2005; Fernandez and Borrok, 2009; Kimball et al., 2009; Mathur et al., 2012; Lv et al., 2016). However, the greywacke lithology of the SQ laterite is sulphide-poor, and neither Cu nor Zn appears to be dominantly hosted in a sulphide phase (Section 5.1).

The alternation of wet and dry seasons results in oscillating reducing and oxic conditions in the developing weathering profile. Under water-saturated conditions, Fe (as ferrous Fe^{2+}) is mobile, while during drier periods this Fe precipitates as ferric Fe oxides, forming the Fe-rich mottles of zone II. Hence, redox changes play an important role in mineral breakdown, the removal of mobile elements, and the formation of secondary minerals enriched in Fe_2O_3 and Al_2O_3. Zinc is not redox active, but mobilization of Cu via Cu(II) reduction has been hypothesised for waterlogged soils and wetland systems (Bigalke et al., 2010c; Bigalke et al., 2013; Babcsányi et al., 2014). However, Cu(II) to Cu(I) reduction is associated with release of the light isotope of Cu (Bigalke et al., 2010c; Bigalke et al., 2013; Babcsányi et al., 2014). The preferential release of light Cu isotopes from host mineral phases via Cu(II) reduction is inconsistent with the isotopically light solid residue observed in the SQ laterite. Hence, though oscillating redox is an important process in lateritization, alone it cannot explain the observed Zn and Cu isotope variations.

In abiotic, proton-promoted dissolution experiments investigating the release of Fe from hornblende, a small light isotope fractionation is observed (Brantley et al., 2001). Similar light isotope fractionation of Fe and Zn is observed during dissolution of granite with HCl (Chapman et al., 2009; Weiss et al., 2014). This preferential release of light isotopes during proton-promoted dissolution likely reflects a kinetic

564 isotope fractionation. Again, preferential mobilization of light isotopes is inconsistent
565 with the isotopically light residue observed in the SQ weathering profile.
566
567 In natural aqueous solutions both Zn and Cu are dominantly complexed to strong
568 organic ligands (McBride, 1981; Coale and Bruland, 1988; e.g., Bruland, 1989; Xue
569 et al., 1995; Moffett and Brand, 1996; Wells et al., 1998; Shank et al., 2004; Grybos
570 et al., 2007; Hoffmann et al., 2007; Vance et al., 2008). It is well documented that
571 mineral dissolution rates are enhanced above proton-promoted rates by the presence
572 of organic ligands, via a ligand-promoted dissolution mechanism (e.g., Berthelin and
573 Munier-Lamy, 1983; Amrhein and Suarez, 1988; Bennett, 1991; Welch and Ullman,
574 1993; 1996; 2000). For example, release of Cu from Columbia River Basalt was
575 elevated in a batch experiment containing an organic ligand (citrate) compared to the
576 inorganic control (Neaman et al., 2005b). At equilibrium, organic complexation is
577 associated with preferential chelation of heavy isotopes (Dideriksen et al., 2008;
578 Jouvin et al., 2009; Bigalke et al., 2010b; Morgan et al., 2010; Fujii and Albarede,
579 2012; Fujii et al., 2013; Sherman, 2013; Fujii et al., 2014; Ryan et al., 2014; Marković
580 et al., 2017). Therefore, at equilibrium, ligand-mediated dissolution should be
581 associated with release of isotopically heavy Zn and Cu, consistent with the observed
582 isotopically light laterite residue.
583
584 We model this scenario as a simple open-system Rayleigh distillation process in
585 Figure 7. In this model, we envisage that the isotopically heavy, organically
586 complexed pool is continuously removed from the profile under a constant
587 fractionation factor. For Zn, the Rayleigh model isotope fractionation factor that best
588 fits the data is of the order $\alpha = 1.0002$, i.e. $\Delta^{66}Zn_{aqueous\text{-}solid} \approx +0.2‰$ (Fig. 7A). For
589 Cu, the required fractionation factor is larger, at about $\alpha = 1.001$ or $\Delta^{65}Cu_{aqueous\text{-}solid} \approx$
590 +1.0‰ (Fig. 7B). The fractionation factors derived from the Rayleigh approach can
591 only be confidently ascribed meaning for a single-step process, e.g., mobilization
592 from the host mineral phase. Several processes are operating and, likely, fractionating
593 Zn and Cu isotopes during lateritization. Nevertheless, the Rayleigh model produces
594 an acceptable fit to the data in spite of its simplicity (Fig. 7), and we proceed to
595 compare our model-derived fractionation factors to those for organic complexation of
596 Zn and Cu in the literature.

The magnitude of Zn and Cu isotope fractionation on organic complexation is a function of the stability constant of complex formation (Ryan et al., 2014; Marković et al., 2017). Organic ligands in freshwater solutions fall into two categories: low molecular weight organic acids (or 'L1-type' ligands, e.g., polyphenols, hydroxamate siderophores), and soluble humic/fulvic acids (Harter and Naidu, 1995). While humic/fulvic acids generally have relatively weak stability constants (at around $\sim 10^7 - 10^9$), L1-type ligands can be much stronger (up to $\sim 10^{25}$). Copper has a particular affinity for strong organic ligands (as compared to, e.g., Zn and Cd; Benedetti et al., 1995; Xue et al., 1995; McBride et al., 1997). Relatedly, the magnitude of isotope fractionation for organic complexation is also larger for Cu compared to Zn (Marković et al., 2017; cf. Ryan et al., 2014).

A fractionation factor $\Delta^{66}Zn_{aqueous\text{-}solid} \approx +0.2‰$ (Fig. 7A) is consistent with an experimental estimate of isotope fractionation for Zn complexation with purified humic acid ($\Delta^{66}Zn_{humic\text{-}aquo} = +0.24 \pm 0.06‰$; Jouvin et al., 2009). By comparison, the larger fractionation factor for Cu ($\Delta^{65}Cu_{aqueous\text{-}solid} \approx +1.0‰$; Fig. 7B) implies complexation by complexes stronger than humic acids, which have a reported range in $\Delta^{65}Cu_{humic\text{-}aquo}$ of +0.24 to + 0.55‰ (Bigalke et al., 2010b; Sherman, 2013; Ryan et al., 2014). Sherman (2013) predicts a fractionation factor for a L1 ligand model complex (Cu acetohydroxamate) of $\Delta^{65}Cu_{hydroxamate\text{-}aquo} = +1.1‰$, while Ryan et al. (2014) measured fractionation factors of up to +0.84‰ for strong synthetic L1-type ligands. Both of these estimates would be consistent with the Rayleigh model prediction.

In practice, it is unclear if chemical equilibrium between the rock and aqueous phase (or something approaching it) can be obtained during weathering. Contrary to the predicted release of heavy isotopes during ligand-promoted dissolution, dissolution of granite in the laboratory in the presence of oxalic acid resulted in release of isotopically *light* Zn (Weiss et al., 2014). Similarly, Brantley et al. (2004) and Wiederhold et al. (2006) observed release of isotopically light Fe in ligand-mediated leaching experiments with hornblende and goethite, respectively. However, these leaching experiments were not at equilibrium, and the observed light isotope fractionation may reflect a kinetic control. By contrast, long duration experiments of

631 Wiederhold et al. (2006) did exhibit the predicted reverse trend, with isotopically
632 heavy Fe in solution. It remains to be determined whether these longer duration
633 experiments more closely reflect processes operating in more advanced (i.e., lateritic)
634 weathering environments.
635
636 Mineral dissolution rates in the lab are typically one to three orders of magnitude
637 faster than in the field (e.g., Swoboda-Colberg and Drever, 1993; Kump et al., 2000;
638 Brantley, 2003). In the lab, dissolution rates are thought to be interface-limited, i.e.
639 the rate of reaction is determined by the dissolution rate of the mineral (Brantley,
640 2003). By contrast, mineral dissolution rates in a transport-limited scenario are
641 controlled by the rate of diffusion or advection in solution (Brantley, 2003). Mineral
642 dissolution is likely predominantly interface-limited in the field (see discussion in
643 Kump et al., 2000), but it can be transport-limited at low water-rock flushing rates
644 (Schnoor, 1990; Kump et al., 2000). This difference may partially explain the offset in
645 lab and field-derived mineral dissolution rates, with transport-limited dissolution
646 operating more slowly than interface-limited dissolution (Kump et al., 2000).
647
648 Lateritic weathering is likely to occur in a transport-limited (also called "supply
649 limited"; West et al., 2005) weathering regime, with low denudation rates coupled to
650 high weathering intensity (White and Buss, 2014). Weathering fluxes in this scenario
651 reflect thermodynamic constraints, with chemical weathering reactions occurring
652 close to equilibrium (White and Buss, 2014). Indeed, this regime is sometimes
653 referred to as 'local-equilibrium' (Lebedeva et al., 2010; Brantley and Lebedeva,
654 2011). Hence, we suggest that transport-limited mineral dissolution may be associated
655 with equilibrium isotope fractionation, while interface-limited mineral dissolution will
656 typically be kinetically controlled (e.g., Brantley et al., 2004; Wiederhold et al., 2006;
657 Weiss et al., 2014). If this hypothesis were correct, ligand-mediated mineral
658 dissolution at equilibrium would promote release of heavy Zn and Cu isotopes,
659 consistent with observations in the SQ laterite (see also section 5.2.2). The corollary
660 of this hypothesis, however, would predict kinetic isotope fractionation (i.e.
661 mobilization of light isotopes) in kinetic-limited (or 'weathering-limited') regimes, in
662 which the physical removal of eroded material is faster than its breakdown by
663 chemical weathering. There is limited evidence for this prediction in Zn and Cu
664 isotope weathering studies to date. We return to this topic in section 5.4.1.

To summarise, the isotopically light compositions observed in the SQ laterite residue may reflect ligand-mediated dissolution of their host phases, if dissolution is occurring close to equilibrium in a transport-limited regime. By contrast, mobilization via either a kinetic or reductive (in the case of Cu) mechanism would be associated with preferential release of isotopically light Zn and Cu. In this case, the salient isotope fractionation during lateritic weathering must occur after Zn and Cu mobilization, in pore waters and/or during precipitation of secondary minerals.

5.2.2 Isotope fractionation in the aqueous phase

As discussed, Zn and Cu will be dominantly complexed by organic ligands in the aqueous phase (e.g., McBride, 1981; Xue et al., 1995; Grybos et al., 2007; Hoffmann et al., 2007), and organic complexation is associated with chelation of heavy Zn and Cu isotopes (Jouvin et al., 2009; Bigalke et al., 2010b; Fujii and Albarede, 2012; Fujii et al., 2013; Sherman, 2013; Fujii et al., 2014; Ryan et al., 2014; Marković et al., 2017). By comparison, the free or weakly complexed pool of Zn or Cu will be isotopically light. Taking Cu as an example, free Cu^{2+} and organically complexed Cu and are isotopically offset by up to –1.1‰ (Sherman, 2013). In a closed system at isotopic equilibrium, the Cu isotope composition of organically complexed Cu (δ_{org}) is constrained by this fractionation factor ($\Delta_{free\text{-}org}$) and the ratio of organically complexed Cu to free Cu (N_{org}/N_{free}), as described by equation 6 (modified after Stevenson et al., 2017):

Eqn 6: $$\delta_{org} = \delta_{system} - \frac{\Delta_{free\text{-}org}}{1+\frac{N_{org}}{N_{free}}}$$

In nature, N_{org}/N_{free} for Cu is always very high – i.e. Cu is almost quantitatively organically complexed. Thus, mass balance constraints dictate that organically complexed Cu in solution will closely reflect the isotopic composition of the Cu that is mobilized during weathering, while the free Cu species will be fractionated by as much as –1.1‰. Consequently, in a scenario in which Zn and Cu are organically complexed in pore waters, secondary mineral phases may simply scavenge the isotopically light uncomplexed (or weakly-complexed) pool of Zn and Cu (as proposed by Vance et al., 2016).

5.2.3 Isotope fractionation during coprecipitation with aluminous Fe oxide

An alternative mechanism to explain the light isotopic composition of the laterite residue is light Zn and Cu isotope fractionation associated with precipitating Fe oxide phases. For example, Viers et al. (2007) observed isotopically light Zn in laterite samples from Cameroon, which they attributed to 'ferrugination', a term which implies preferential incorporation or sorption of light isotopes in or on precipitating Fe oxide phases. Suhr et al. (2018) suggested a similar process to explain isotopically light Zn in the residue of a basaltic laterite from Bidar, India. We observe negative correlations of δ^{66}Zn and δ^{65}Cu with Fe_2O_3 (Fig. 8), indicating that Fe oxide formation may well play a role in the very light isotopic compositions of Cu and Zn in zone II and IV samples.

Can ferrugination alone lead to isotopically light Zn and Cu in the laterite residue? Most experimental studies have focussed upon inorganic *sorption* of Zn and Cu on Fe oxide (or other mineral) surfaces, with the prevailing paradigm that such sorption is typically associated with preferential accumulation of heavy isotopes on the mineral surface (Pokrovsky et al., 2005; Balistrieri et al., 2008; Juillot et al., 2008; Pokrovsky et al., 2008; Bryan et al., 2015; Guinoiseau et al., 2016). Preferential sorption of heavy isotopes on precipitating oxide surfaces would be contrary to the observed light isotopic compositions of laterite samples in zones II and IV.

The dominant Fe oxide phases present in the SQ samples are aluminous goethite and aluminous haematite (Table S1; Wimpenny et al., 2007). Both phases can also *incorporate* Zn^{2+} and Cu^{2+} into their structures, via substitution for Fe^{3+} on octahedral (VI-fold coordinated) sites (e.g., Cornell and Giovanoli, 1988; Gerth, 1990; Manceau et al., 2000; Cornell and Schwertmann, 2003). Incorporation of significant Zn (19.9 μg/g) and Cu (31 μg/g) in goethite and haematite, comparable to the concentrations observed in the indurated SQ duricrust (Zn: 25 – 31 μg/g, Cu: 39 – 61 μg/g), has been suggested for lateritic samples from Western Australia (Anand and Gilkes, 1987; Singh and Gilkes, 1992). Preferential incorporation of isotopically light Zn and Cu into precipitating aluminous Fe oxides could thus provide a mechanism to drive the laterite residue isotopically light.

732 The trajectory of the dashed arrow in Figure 9A implies a maximum effective isotopic
733 fractionation factor on incorporation of Zn into Fe oxides of $\Delta^{66}Zn_{\text{Fe oxide-aqueous}} \approx -$
734 0.7‰ (Fig 9A). A conference abstract indicates that Zn incorporation in goethite may
735 indeed be associated with a preference for the light Zn isotope, though the magnitude
736 of associated isotope fractionation is not reported (Becker et al., 2014). In the case of
737 Cu, the equivalent maximum effective isotope fractionation factor described by the
738 trajectory of the dashed arrow in Figure 9B is about –1.3‰. Experiments measuring
739 isotope fractionation on incorporation of trace metals in Fe (and other, e.g., Al) oxides
740 are an important avenue for future research.
741
742 To conclude, we postulate that a combination of strong complexation by organic
743 ligands in association with the retention of light isotopes in or on secondary
744 aluminous Fe oxide phases can explain the residual light Zn and Cu isotope signatures
745 of the zone II and IV laterite samples. If ferrugination alone is driving the light
746 isotopic composition of the laterite residue, Zn and Cu must be incorporated in (rather
747 than sorbed on) Fe oxide phases. Micro-analytical techniques, such as EXAFS, may
748 allow identification of the phase association and crystal chemistry of Zn and Cu in
749 laterite samples.
750
751 *5.2.4 Upper horizon: a role for organic matter?*
752
753 Surface organic-rich layers of soils are often enriched in light Zn and Cu isotopes,
754 which has been related to the uptake and recycling of plants (e.g., Bigalke et al., 2011,
755 2010a; Liu et al., 2014; Vance et al., 2016; Weiss et al., 2007). Therefore, the
756 presence of isotopically light solid organic matter in the uppermost sample of the SQ
757 weathering profile is plausible, given that the surface of the lateritic mesa into which
758 the quarry has been excavated is characterized by well-developed sub-tropical scrub
759 vegetation, predominantly acacia. The uppermost sample (SQ14) is slightly enriched
760 in Cu and Zn relative to the other two indurated laterite duricrust samples (SQ12 and
761 SQ13), and is indeed the isotopically lightest sample in the whole section ($\delta^{66}Zn = -$
762 0.02‰ and $\delta^{65}Cu = -0.89$‰; Figs. 3 and 4). Unfortunately, we lack sufficient
763 sampling resolution to evaluate in detail the role of recent biological activity and
764 modern soil formation in the uppermost meters of the weathering profile.
765

766 **5.3 Zone III: the Paleo-water Table**

767

768 Previous studies have noted considerable major and trace element and isotope
769 variability associated with the paleo-water table zone III (at 7 – 8.5 m depth, samples
770 SQ10 and SQ11; Howarth et al., 2018; Wimpenny et al., 2007; Widdowson, 2009),
771 which represents a transition from sub-oxic to fully oxidising conditions (Wimpenny
772 et al., 2007). There are two ways of interpreting this zone of alteration. To date, it has
773 been suggested to be at the top of a 'classic' groundwater level that was abandoned
774 during uplift (Wimpenny et al., 2007). As such, it is considered to have developed
775 through a combination of open system, allochthonous input of trace elements from
776 circulating groundwaters, and the precipitation of Fe and Mn-oxides, which act as
777 effective scavengers of other elements (Howarth et al., 2018; Wimpenny et al., 2007;
778 Widdowson, 2009).

779

780 An alternative interpretation suggests that zone III was at the base of an ancient,
781 episodic stagnant water body (i.e. seasonally present between the surface and ~8 m
782 depth). In this case, water would have accumulated at a depth with reduced water
783 permeability at the base of zone III during the rainy season, and zones III and IV
784 could be considered together as a single lateritized package that subsequently
785 underwent uplift, drying and hardening to form the present duricrust. In this scenario,
786 the Fe-rich mottles in zone II (i.e. at depths below ~8 m) would reflect a second phase
787 of waterlogging and lateritization, with seasonal stagnant water pooling close to the
788 present day line of seepage (at ~15 m depth). This idea, of two repeating packages of
789 lateritic alteration, could plausibly explain the τ_{Zn}, τ_{Cu} and Zn and Cu isotope data
790 (Figs. 4B, 5A). However, we would expect to observe Fe enrichment at the line of
791 seepage, equivalent to that observed in zone III (Fig. 4C), and no such Fe (or Mn)
792 enrichment is observed. Further sampling at higher resolution, and laterally within the
793 quarry, would help reconcile these two scenarios. For the purpose of this study, we
794 consider that the distinct geochemistry of the samples in zone III deserve separate
795 treatment to the more predictable upwardly progressing alteration characteristics of
796 the remainder of the profile.

797

798 Evidence for the allochthonous input of elements to zone III is demonstrated through
799 the behaviour of τ_{Fe} and τ_{Mn} values (Fig. 4C, Table 2). Both τ_{Fe} (18.9) and τ_{Mn} (5.5)

800 show extreme enrichment at 7.5m (SQ11), while τ_{Fe} (4.6) is also considerably
801 enriched at 8.5m (SQ10). The allochthonous input of elements to the profile can be
802 quantified by calculating integrated τ-values, weighting taus for each horizon (h) by
803 density (ρ) and thickness (z), following Vance et al. (2016):
804 Eqn. 6: $\tau_i^{int} = \frac{\sum_{h=0}^{n}(\tau_h \rho_h z_h)}{\sum_{h=0}^{n}(\rho_h z_h)}$
805 where i refers to the element of interest (Zn or Cu). This approach assumes negligible
806 denudation (physical erosion) of the weathering profile during development.
807
808 Positive integrated τ_{Fe}^{int} (1.5) and, marginally, τ_{Mn}^{int} (0.02) values (Table 2), suggest that
809 the zone III enrichments in τ_{Fe} and τ_{Mn} cannot simply be explained by redistribution
810 of these elements vertically (from zone II or IV, depending on the location of the
811 water body) in the weathering profile. If we assume allochthonous input of Fe and Mn
812 at the paleo-water table depths and exclude these zone III samples from the integrated
813 τ calculations (giving $\tau_i^{int\text{-}III}$ values), we find a negative integrated $\tau_{Mn}^{int\text{-}III}$ (–0.21) value,
814 consistent with that calculated for $\tau_{Li}^{int\text{-}III}$ (–0.21) and $\tau_{Zn}^{int\text{-}III}$ (–0.22). $\tau_{Fe}^{int\text{-}III}$ remains
815 positive, however, at 0.36, suggesting 30 to 40% Fe addition to the weathering profile
816 during alteration.
817
818 Both Cu (52 μg/g) and Zn (97 μg/g) show enrichment in zone III, with τ_{Cu} = 0.8 and
819 τ_{Zn} = 0.5 at 7.5m (SQ11, Fig. 4B). Integrated τ_{Zn}^{int} and τ_{Cu}^{int} values are negative,
820 however, both including (τ_{Zn}^{int} = –0.23, τ_{Cu}^{int} = –0.07) and excluding ($\tau_{Zn}^{int\text{-}III}$ = –0.22,
821 $\tau_{Cu}^{int\text{-}III}$ = –0.06) the zone III samples (Table 2). Therefore, the enrichments of Zn and
822 Cu in zone III do not *require* an allochthonous source of these two elements, though
823 such a source is not excluded.
824
825 The enrichments in Cu and Zn in zone III are restricted to a narrow depth range,
826 sampled at SQ11 only (7.5m, Fig. 4B). This pattern is similar to the narrow band of
827 enrichment observed for Mn (Fig. 4C) and contrasts with that of Fe, which is
828 significantly elevated across both SQ10 and SQ11 (8.5 – 7.5m; Fig. 4C). Manganese
829 oxide develops large areas of negative charge under the pH conditions of natural
830 waters, as a consequence of its low pH point of zero charge and relatively high
831 specific surface area (Catts and Langmuir, 1986). These characteristics make it a very

effective sorbent for other trace metals (e.g., Aplin and Cronan, 1985; Balistrieri and Murray, 1986; Koschinsky and Hein, 2003; Peacock and Sherman, 2007; Tessier et al., 1996). Accordingly, we suggest that Cu and Zn are scavenged by a precipitating Mn oxide phase at the paleo-water table, rather than by the abundant Fe oxide phases (as suggested for the zone II and IV samples; section 5.2). Sequential leaching experiments would be required to further test this hypothesis.

Sample SQ11 is marked by an excursion towards isotopically heavier Cu compared to the samples below and above, indicating scavenging of heavy Cu (Figs. 5, 7). In the case of Zn, there is no resolvable shift in δ^{66}Zn (at +0.14‰) compared to the samples above and below. In both cases sample SQ11 is distinct from the coherent τ–δ trends observed throughout the rest of the profile, which are reasonably well described by a simple Rayleigh model (as described in Section 5.2.1; Fig. 7). There are two possible explanations for the enrichment and distinct isotopic composition of SQ11: first, a source with an isotopically heavy Cu isotope composition, or second, a source combined with *in situ* isotope fractionation on sorption to the postulated Mn-oxide phase.

Aerosols are one possible external source of trace metals to weathering profiles, and are typically approximately lithogenic in Zn and Cu isotope composition (δ^{66}Zn ~0.3‰ and δ^{65}Cu ~0‰; Dong et al., 2013; Little et al., 2014b). Based on the data in this study, a locally derived lateritic aerosol source would be very isotopically light, however, inconsistent with the shift toward heavier Cu isotope compositions at the depth of the paleo-water table. Further, assuming an atmospheric route for aerosol deposition, any aerosol addition should also be apparent as enrichment at the surface-most depths of the laterite profile; such behaviour is not observed for the SQ profile.

Solute-laden groundwater has previously been suggested as providing an external source of Re, Os, and Tl, to the SQ laterite, possible due to its low-lying topographic position (Howarth et al., 2018; Wimpenny et al., 2007). Relatively few constraints exist on the isotopic composition of Zn and Cu in groundwater, however. An isotopically heavy groundwater source of Cu is certainly plausible, given observations of isotopically heavy Cu in the dissolved phase in rivers (+0.02 to +1.45‰, discharge-weighted average of +0.68‰; Vance et al., 2008). A groundwater-borne source of Zn

at about +0.2‰ is also possible, given the range of dissolved $\delta^{66}Zn$ in global rivers (–0.12 to +0.88‰, discharge-weighted average of +0.33‰; Little et al., 2014b) and mountain streams (+0.02 to +0.46‰, Borrok et al., 2008). Future isotope studies should target groundwater in conjunction with surface-flowing water bodies.

Isotope fractionation may occur on sorption to the postulated Mn oxide phase. Bryan et al. (2015) investigated Zn isotope fractionation on inorganic sorption to synthetic birnessite (δ-MnO_2), a phyllomanganate phase common in terrestrial environments (e.g., Taylor et al., 1964; Ross et al., 1976; Tokashiki et al., 1986; Uzochukwu and Dixon, 1986; Post, 1999). At low ionic strength (applicable to freshwater environments) they observe negligible Zn isotope fractionation, which is attributed to the formation of octahedral surface complexes (Manceau et al., 2002); i.e. there is no marked change in coordination environment on sorption compared to the hydrated $Zn(H_2O)_6^{2+}$ ion present in solution (Bryan et al., 2015). Sorption of ~V-fold coordinated hydrated Cu^{2+} on δ-MnO_2 is predicted to be associated with an enrichment in heavy isotopes, due to the formation of tetrahedral surface complexes (Manceau et al., 2002; Sherman and Peacock, 2010; Little et al., 2014a), though an experimental study observed the opposite: preferential sorption of light Cu isotopes on δ-MnO_2 ($\Delta^{65}Cu_{MnO2\text{-}aqueous} = -0.45 \pm 0.18$‰, n=12; Ijichi et al., 2018).

As described, the paleo-water table sample SQ11 is unusual in that it is unfractionated in $\delta^{66}Zn$ and isotopically heavy in $\delta^{65}Cu$ compared to the samples above and below, thus partly consistent with these inorganic predictions for sorption of hydrated Zn^{2+} and Cu^{2+} on δ-MnO_2. However, the system is underconstrained: we lack information about the isotopic composition of the contemporaneous fluid. Speciation in the natural environment is more complex compared to these inorganic experimental and theoretical considerations. In future, more realistic models and experiments should be designed that incorporate mixtures of organic and inorganic ligands and analogue mineral surfaces.

To summarise, the distinctive Fe and Mn enrichment of the paleo-water table samples supports the suggestion of open system behaviour in this zone (Wimpenny et al., 2007). The observed Zn and Cu enrichment could be explained by mobilisation from zones II or IV of the weathering profile or an additional groundwater-borne source,

with scavenging on precipitating oxide phases. Specifically, we suggest that Cu and Zn are primarily scavenged by a Mn oxide phase at 7.5m depth, consistent with previously published Tl isotope evidence (Howarth et al., 2018).

5.4 Synthesis: Cu and Zn isotopes in the weathering environment

5.4.1 Integrated weathering profiles and isotope fractionation during weathering

To draw broader conclusions regarding the behaviour of Cu and Zn during lateritization, and weathering in general, we compare integrated τ-values and isotopic compositions from weathering and soil profiles from diverse localities. To facilitate this comparison, we normalise weathered delta values to the presumed parent material (where, e.g., $\Delta^{66}Zn = \delta^{66}Zn_{parent} - \delta^{66}Zn_{sample}$) and calculate integrated $\Delta^{66}Zn_{int}$ and $\Delta^{65}Cu_{int}$ values (Table 2) for the entire weathering profile in the same fashion as used to calculate integrated τ-values (Eqn. 6).

The SQ laterite profile shows an integrated loss of Zn of –23%, with an integrated $\Delta^{66}Zn_{int}$ of –0.14‰ (Table 2). These SQ τ–Δ data are plotted alongside data from the literature in Figure 9, updating the compilation in Moynier et al. (2017, their Fig. 11). Overall, Zn-depleted (negative τ_{Zn}) weathering profiles and soils show limited isotope fractionation from the parent lithology. However, at the highest degrees of chemical weathering, above ~70% Zn depletion compared to the protolith, significant preferential loss of heavy Zn isotopes in three different lateritic weathering profiles is observed (from India: Suhr et al., 2018 and this study; from Cameroon: Viers et al., 2007).

For Cu, a smaller integrated loss of –7% from the SQ profile is calculated, with a more negative $\Delta^{65}Cu_{int}$ of –0.32‰ (Table 2). There is considerably more scatter in the τ_{Cu} – $\Delta^{65}Cu$ plot (Fig. 9B) – likely due to the multiple potential processes influencing Cu isotopes and to more heterogeneous protolith Cu concentrations. However, nearly all Cu-depleted profiles show negative $\Delta^{65}Cu_{int}$ values (plotting in the lower left

quadrant of Fig. 9B), indicating consistent loss of isotopically heavy Cu during weathering.

Two plausible explanations for the release of isotopically heavy Zn and Cu during lateritic weathering have been discussed: (1) incorporation of light isotopes in aluminous Fe oxide phases (ferrugination) or (2) organic complexation of heavy isotopes in the dissolved phase. In section 5.2.1, we suggested that organic complexation might lead to mobilization of heavy isotopes if mineral dissolution approaches chemical equilibrium, and that this scenario would be plausible in a transport-limited weathering regime. However, Figure 9 does not provide evidence for the converse prediction – of mobilization of light Cu (or Zn) isotopes in kinetically controlled, weathering-limited regimes (Fig. 9). Alternatively, in section 5.2.2, we suggested that organic complexation retains heavy isotopes in the aqueous phase *after* mobilization of Cu and Zn from their host mineral phases, with sorption of the complementary light pool on secondary Fe oxide minerals (section 5.2.2).

It is notable that Cu isotope data from weathering profiles developed on different lithologies fall on a similar fractionation trend (Fig. 9B, dashed arrow). Mathur et al. (2012) and Lv et al. (2016) favour oxidative weathering of Cu sulphides to explain residual isotopically light Cu signatures observed in weathered black shales. Given the absence of Cu-hosting sulphide phases in the SQ laterite, we propose that a combination of organic complexation in the aqueous phase and retention of light isotopes by secondary precipitating Fe oxide phases is the most likely explanation for the release of heavy Cu (and Zn) isotopes during lateritization. At greater degrees of Cu loss (>80%), Vance et al. (2016) observe a return towards protolith Cu isotope compositions in a sequence of increasingly waterlogged basaltic soils in Hawaii (Fig. 9B, dotted arrow), which they attribute to reduction of Fe oxides and return of the associated isotopically light Cu to the aqueous phase.

5.4.2 Implications for the weathering-derived flux of Zn and Cu to rivers on geological timescales

The sensitivity of the global cycles of Zn and Cu to a change in the riverine flux depends on the magnitude and timescale of the change compared to the residence time

966 of the element in the ocean. In the modern ocean, both Zn and Cu have relatively
967 short residence times of a few thousand years (Hayes et al., 2018 and references
968 therein). Thus, there is scope to influence the global ocean budgets of Zn and Cu via a
969 change in the riverine input. There are two possible ways to influence the isotopic
970 composition of the weathering-derived input of Zn and Cu to rivers: (1) change the
971 isotopic composition of the predominant weathered lithology and (2) change the
972 intensity of weathering and any associated isotope fractionation. The former is
973 unlikely to be a major control, because clastic sediments and igneous rocks have
974 restricted Zn and Cu isotope compositions (Moynier et al., 2017) and because there is
975 no consistent relationship between riverine δ^{66}Zn or δ^{65}Cu and catchment lithology in
976 modern dissolved phase river data (Vance et al., 2008; Little et al., 2014b). In this
977 contribution, we set out to address the latter, i.e. what is the maximum leverage of
978 chemical weathering on the isotopic composition of Zn and Cu supplied to rivers?
979
980 Figure 9A illustrates that significant weathering-derived Zn isotope fractionation only
981 occurs during extreme chemical weathering (lateritization). Lateritization was
982 promoted during Greenhouse climate periods of Earth history (e.g., the mid Miocene
983 Climatic Optimum), with the mid Tertiary to mid Quaternary considered to be a
984 period of particularly intensive chemical weathering (e.g., Dalvi et al., 2004; Thorne
985 et al., 2012; Widdowson, 2009). Could such a shift in weathering style have an impact
986 on the riverine δ^{66}Zn signature? While our data indicate that the Zn isotope
987 composition of the instantaneous flux to rivers from lateritic terrains can change, we
988 suggest that even widespread lateritization is unlikely to have had a major impact on
989 global average riverine δ^{66}Zn. At the very high degrees of Zn mobility observed
990 during lateritic weathering, the isotopic composition of the cumulative aqueous phase
991 will approach that of the protolith by mass balance. Thus, the average Zn isotope
992 composition of the source of Zn to rivers should be rather insensitive to climate-
993 driven change on geological timescales. Nevertheless, the scope for an instantaneous
994 change in the riverine flux should be considered on short timescales and at local and
995 regional spatial scales.
996
997 The small but growing dataset for Cu isotopes during weathering indicates release of
998 isotopically heavy Cu in all oxygenated environments (Fig. 9B), consistent with the
999 observed isotopically heavy Cu in the dissolved phase of modern rivers (Vance et al.,

2008). In contrast, weathering in modern reducing environments appears to re-release isotopically light Cu associated with Fe-Mn oxides (Fig. 9B; Vance et al., 2016). Periodic flooding may also lead to reduction of Cu(II) to Cu(I), with release of isotopically light Cu(I) to the aqueous phase (Bigalke et al., 2010c; Bigalke et al., 2013; Babcsányi et al., 2014). Generally, however, Cu mobility during chemical weathering is likely to be significantly reduced under anoxic conditions (e.g., Neaman et al., 2005a, 2005b). Copper and Cu isotopes may therefore be an interesting marker for the presence or absence of oxygen during the development of paleosols.

Finally, release of isotopically heavy Cu during weathering is consistent with the scenario outlined by Chi Fru et al. (2016) for an observed shift from relatively low to higher δ^{65}Cu values in marine sediments across the great oxidation event (GOE). This shift was interpreted to reflect release of isotopically heavy Cu from the continents on the establishment of oxidative weathering (Chi Fru et al., 2016). These authors favoured oxidative weathering of sulphides as the primary mechanism responsible for releasing heavy Cu, while our study emphasizes that weathering in an oxygenated environment promotes retention of light Cu and release of heavy Cu, regardless of the primary host phase.

6.0 Conclusions

We have presented evidence of systematic and correlated Zn and Cu isotope fractionation during lateritization, observing retention of light isotopes in the associated weathering profile. Zinc and Cu in the residue are likely incorporated in secondary aluminous Fe oxide phases in the laterite, a process of 'ferrugination' that may itself be accompanied by isotope fractionation. Alternatively, the precipitating Fe oxide phases may passively scavenge light isotopes due to preferential organic complexation of heavy isotopes in the aqueous phase. The relative roles of organic complexation versus incorporation in Fe oxide phases, and their interaction with the multitude of other controls on metal speciation in the weathering environment (e.g., presence of inorganic ligands, pH, redox, solid organic matter) are an important target for future experimental and theoretical work.

Our study, taken together with those previously published, illustrates that Zn isotope fractionation during weathering is limited, except at very extreme degrees of Zn removal. Therefore, mass balance constraints limit the impact of isotopic fractionation at high degrees of chemical weathering on the $\delta^{66}Zn$ of the riverine flux. This inference is consistent with the modern measured average $\delta^{66}Zn$ in rivers, which is unfractionated from the lithogenic $\delta^{66}Zn$ value.

In contrast, weathering of all lithologies studied to date appears to be associated with preferential retention of isotopically light Cu, consistent with isotopically heavy Cu in the dissolved pool of rivers. Weathering alone cannot account for the isotopically heavy riverine flux on long timescales, however, due to the relatively small pool of light Cu stored in terrestrial reservoirs like soils (Vance et al., 2016). Likely, the processes responsible for the liberation of heavy Cu during weathering (or, conversely, the retention of light Cu) continue to operate in some form downstream, with partitioning between the dissolved and particulate phase maintained in rivers and the oceans.

Acknowledgements

The authors would like to thank four reviewers and particularly the associate editor, Matthew Fantle, for wide-ranging comments that significantly improved the original manuscript. SHL is grateful for financial support from the Leverhulme Trust (ECF-2014-615) and NERC (NE/P018181/1). This manuscript builds on the 4th year MSci project of SM at Imperial College London. We acknowledge helpful discussions with David Wilson, Dominik Weiss, Nils Suhr, Derek Vance and Brandi Revels. We are grateful to Katharina Kreissig for laboratory support and Mark Rehkämper for supplying the Zn DS. MW gratefully acknowledges Orlando Fernandes (Dhempe College, Miramar, Goa), and Sridhar Iyer (NIO, Dona Paula, Goa) for their support during fieldwork.

Figure Captions

Figure 1. **Left**: The location of Goa state (red) on the Indian Dharwar Craton (adapted from Paton et al., 2007). In the northeastern corner of the state, Deccan Trap flood basalts overlie the Dharwar metasediments. **Right**: The geology of Goa state (adapted from Widdowson, 2009; Devaraju et al., 2010). The black dashed line represents the state boundary. The Merces Quarry (SQ) laterite profile (labelled) is located at 15°28'44"N, 73°52'35"E. It is developed on Dharwar Late Archaean biotite-bearing greywacke.

Figure 2. Left: Schematic illustrating the depth distribution of samples in the laterite profile in relation to characteristic zones of alteration (Wimpenny et al., 2007; Widdowson, 2009). Graphs from left to right: Major element concentration variations (SiO_2, Al_2O_3, Fe_2O_3; Widdowson, 2009), MnO concentration variations (Widdowson, 2009), and indices of alteration (Chemical Index of Alteration, CIA; Index of Lateritization, IOL; see text for further details). Grey shading highlights zone III, the paleo-water table. Samples showing only limited alteration, from below the dotted line of seepage (zone I), are paler in colour.

Figure 3. The crystal abundances of major mineral phases in the SQ laterite weathering profile compared to the four identified zones of alteration (Fig. 2; Wimpenney et al., 2007).

Figure 4. A. Concentration profiles and **B.** τ enrichment-depletion profiles (see text for details) of Li (grey triangles), Zn (red squares) and Cu (blue diamonds) in the SQ profile. C. τ enrichment-depletion profiles for Fe and Mn. Open symbols: little altered samples in zone I, below line of seepage (dotted line). Filled symbols: altered samples in zones II-IV, above line of seepage. Grey shaded zone III has been influenced by the paleo-water table.

Figure 5. A. Depth profiles of $\delta^{66}Zn$ (red squares) and $\delta^{65}Cu$ (blue diamonds). Open symbols: unaltered-little altered samples in zone I, below line of seepage (dotted line). Filled symbols: very increasingly altered zone II-IV mottled and lateritic samples.

Shaded grey rectangle: zone III, influenced by the paleo-water table. **B.** Positive correlation between $\delta^{66}Zn$ and $\delta^{65}Cu$ in the SQ profile. Linear regression (arrow) indicates coupled loss of heavy Cu and Zn isotopes during lateritization and a resultant shift towards residual isotopically light values. Error bars represent long-term external 2SD reproducibility.

Figure 6. Covariation of Zn and Cu with selected major (A-D) and trace elements (E-H) in samples from zone I (unaltered – little altered) of the SQ laterite profile. Positive correlations of Zn with elements commonly hosted in biotite (Mg, K, Li, Co and Rb) suggest that Zn is primarily hosted in biotite in the parent greywacke (see also Fig. S3). Copper shows negative correlations with most other major and trace elements, with the exception of SiO_2 and Na_2O (Panel D), suggesting an association with a detrital phase.

Figure 7. Rayleigh fractionation modelling of **A**. Zn and **B.** Cu isotopes assuming preferential mobilization of heavy isotopes to the dissolved phase, assuming $R = R_0 . f^{\alpha - 1}$ (where R_0 is the isotope ratio of the protolith (larger open symbols), f the fraction removed and α the fractionation factor. For Zn: $\alpha = 1.0002$, for Cu: $\alpha = 1.001$). Dashed line: residual isotopic composition of the solid. Dash-dotted line: cumulative isotopic composition of the fluid removed from the system. Dotted line: instantaneous fluid isotopic composition. Symbols as in Figures 4 and 6. Error bars represent long-term external 2SD reproducibility. Paleo-water table sample SQ11 labelled.

Figure 8. Negative correlations of $\delta^{66}Zn$ (red squares) and $\delta^{65}Cu$ (blue diamonds) with Fe_2O_3 in the SQ profile. Paleo-water table sample SQ11 circled, other symbols as in Figure 4. Regressions are shown excluding (solid lines) and including (dashed lines) SQ11. Error bars represent long-term external 2SD reproducibility.

Figure 9. Integrated τ and integrated isotopic compositions for global weathering profiles **A**. Zn and **B**. Cu. Note, data are only included for studies where τ values are reported or can be calculated (Viers et al., 2007; Mathur et al., 2012; Liu et al., 2014; Lv et al., 2016; Vance et al., 2016). In order to include as much data as possible, but where an integrated τ-value cannot be calculated because horizon depths are not reported, either the full profile (for the central China black shale; Lv et al., 2016) or

1130 the mean and 1SD for each published profile (for the Cameroon laterite profiles; Viers
1131 et al., 2007) is shown. The SQ laterite dataset is shown as a full profile and as an
1132 integrated signature (larger symbol). Recently published full profile Zn isotope data is
1133 also included for the Bidar laterite, developed on Deccan basalt, for comparison (Zn
1134 only: Suhr et al., 2018). Literature data: [1] Viers et al. (2007), [2] Suhr et al. (2018),
1135 [3] Vance et al. (2016), [4] Lv et al. (2016), [5] Liu et al. (2014), [6] Mathur et al.
1136 (2012).
1137
1138

References

Aleva G. J. (1984) Lateritization, bauxitization and cyclic landscape development in the Guiana Shield. *Bauxite*, 297–318.

Amrhein C. and Suarez D. L. (1988) The use of a surface complexation model to describe the kinetics of ligand-promoted dissolution of anorthite. *Geochim. Cosmochim. Acta*.

Anand R. R. and Gilkes R. J. (1987) Iron oxides in lateritic soils from Western Australia. *Eur. J. Soil Sci.* **38**, 607–622.

Aplin A. C. and Cronan D. S. (1985) Ferromanganese oxide deposits from the Central Pacific Ocean, I. Encrustations from the Line Islands Archipelago. *Geochim. Cosmochim. Acta* **49**, 427–436.

Archer C. and Vance D. (2004) Mass discrimination correction in multiple-collector plasma source mass spectrometry: an example using Cu and Zn isotopes. *J. Anal. At. Spectrom.* **19**, 656. Available at: http://xlink.rsc.org/?DOI=b315853e.

Archer C. and Vance D. (2008) The isotopic signature of the global riverine molybdenum flux and anoxia in the ancient oceans. *Nat. Geosci.* **1**, 597–600.

Argast S. and Donnelly T. W. (1986) Compositions and sources of metasediments in the upper Dharwar Supergroup, South India. *J. Geol.* **94**, 215–231.

Arnold T., Schönbächler M., Rehkämper M., Dong S., Zhao F. J., Kirk G. J. D., Coles B. J. and Weiss D. J. (2010) Measurement of zinc stable isotope ratios in biogeochemical matrices by double-spike MC-ICPMS and determination of the isotope ratio pool available for plants from soil. *Anal. Bioanal. Chem.* **398**, 3115–3125.

Babcsányi I., Imfeld G., Granet M. and Chabaux F. (2014) Copper stable isotopes to trace copper behavior in wetland systems. *Environ. Sci. Technol.* **48**, 5520–5529.

Babechuk M. G., Widdowson M. and Kamber B. S. (2014) Quantifying chemical weathering intensity and trace element release from two contrasting basalt profiles, Deccan Traps, India. *Chem. Geol.* **363**, 56–75. Available at: http://dx.doi.org/10.1016/j.chemgeo.2013.10.027.

Balistrieri L. S., Borrok D. M., Wanty R. B. and Ridley W. I. (2008) Fractionation of Cu and Zn isotopes during adsorption onto amorphous Fe(III) oxyhydroxide: Experimental mixing of acid rock drainage and ambient river water. *Geochim. Cosmochim. Acta* **72**, 311–328.

1172 Balistrieri L. S. and Murray J. W. (1986) The surface chemistry of sediments from the
1173 Panama Basin: The influence of Mn oxides on metal adsorption. *Geochim*.
1174 *Cosmochim*. *Acta* **50**, 2235–2243.
1175 Banks N. G. (1973) Biotite as a source of some of the sulfur in porphyry copper
1176 deposits. *Econ*. *Geol*. **68**, 697–703.
1177 Becker K., Catalano J. and Moynier F. (2014) Connecting Zinc Partitioning and
1178 Isotope Fractionation during Fe(II)-Catalyzed Recrystallization of Fe(III) Oxide
1179 Minerals. In *Goldschmidt Abstracts* p. 151.
1180 Benedetti M. F., Milne C. J., Kinniburgh D. G., Van Riemsdijk W. H. and Koopal L.
1181 K. (1995) Metal Ion Binding to Hemic Substances: Application of the Non-Ideal
1182 Competitive Adsorption Model. *Environ*. *Sci*. *Technol*. **29**, 446–457.
1183 Bennett P. C. (1991) Quartz dissolution in organic-rich aqueous systems. *Geochim*.
1184 *Cosmochim*. *Acta*.
1185 Bentahila Y., Othman D. Ben and Luck J.-M. (2008) Strontium, lead and zinc
1186 isotopes in marine cores as tracers of sedimentary provenance: A case study
1187 around Taiwan orogen. *Chem*. *Geol*. **248**, 62–82.
1188 Berthelin J. and Munier-Lamy C. (1983) Microbial Mobilization and Preconcentration
1189 of Uranium from Various Rock Materials by Fungi. *Ecol*. *Bull*., 395–401.
1190 Available at: http://www.jstor.org/stable/20112875.
1191 Bigalke M., Kersten M., Weyer S. and Wilcke W. (2013) Isotopes trace
1192 biogeochemistry and sources of Cu and Zn in an intertidal soil. *Soil Sci*. *Soc*. *Am*.
1193 *J*. **77**, 680–691.
1194 Bigalke M., Weyer S., Kobza J. and Wilcke W. (2010a) Stable Cu and Zn isotope
1195 ratios as tracers of sources and transport of Cu and Zn in contaminated soil.
1196 *Geochim*. *Cosmochim*. *Acta* **74**, 6801–6813. Available at:
1197 http://dx.doi.org/10.1016/j.gca.2010.08.044.
1198 Bigalke M., Weyer S. and Wilcke W. (2010b) Copper isotope fractionation during
1199 complexation with insolubilized humic acid. *Environ*. *Sci*. *Technol*. **44**, 5496–
1200 5502.
1201 Bigalke M., Weyer S. and Wilcke W. (2010c) Stable copper isotopes: A novel tool to
1202 trace copper behavior in hydromorphic soils. *Soil Sci*. *Soc*. *Am*. *J*. **74**, 60.
1203 Bigalke M., Weyer S. and Wilcke W. (2011) Stable Cu isotope fractionation in soils
1204 during oxic weathering and podzolization. *Geochim*. *Cosmochim*. *Acta* **75**, 3119–
1205 3134. Available at: http://dx.doi.org/10.1016/j.gca.2011.03.005.

1206 Bonnet N. J., Beauvais A., Arnaud N., Chardon D. and Jayananda M. (2014)
1207 First40Ar/39Ar dating of intense Late Palaeogene lateritic weathering in
1208 Peninsular India. *Earth Planet*. *Sci*. *Lett*. **386**, 126–137. Available at:
1209 http://dx.doi.org/10.1016/j.epsl.2013.11.002.
1210 Borrok D. M., Nimick D. A., Wanty R. B. and Ridley W. I. (2008) Isotopic variations
1211 of dissolved copper and zinc in stream waters affected by historical mining.
1212 *Geochim*. *Cosmochim*. *Acta* **72**, 329–344.
1213 Brantley S. L. (2003) Reaction Kinetics of Primary Rock-forming Minerals under
1214 Ambient Conditions. In *Treatise on Geochemistry* (eds. H. D. Holland and K. K.
1215 Turekian). Elsevier. pp. 73–117.
1216 Brantley S. L. and Lebedeva M. (2011) Learning to Read the Chemistry of Regolith
1217 to Understand the Critical Zone. *Annu*. *Rev*. *Earth Planet*. *Sci*. **39**, 387–416.
1218 Available at: http://www.annualreviews.org/doi/10.1146/annurev-earth-040809-
1219 152321.
1220 Brantley S. L., Liermann L. and Bullen T. D. (2001) Fractionation of Fe isotopes by
1221 soil microbes and organic acids. *Geology*.
1222 Brantley S. L., Liermann L. J., Guynn R. L., Anbar A., Icopini G. A. and Barling J.
1223 (2004) Fe isotopic fractionation during mineral dissolution with and without
1224 bacteria. *Geochim*. *Cosmochim*. *Acta* **68**, 3189–3204.
1225 Bridgestock L. J., Williams H., Rehkämper M., Larner F., Giscard M. D., Hammond
1226 S., Coles B., Andreasen R., Wood B. J. and Theis K. J. (2014) Unlocking the
1227 zinc isotope systematics of iron meteorites. *Earth Planet*. *Sci*. *Lett*. **400**, 153–
1228 164.
1229 Bruland K. W. (1989) Complexation of zinc by natural organic ligands in the central
1230 North Pacific. *Limnol*. *Oceanogr*. **34**, 269–285.
1231 Bryan A. L., Dong S., Wilkes E. B. and Wasylenki L. E. (2015) Zinc isotope
1232 fractionation during adsorption onto Mn oxyhydroxide at low and high ionic
1233 strength. *Geochim*. *Cosmochim*. *Acta* **157**, 182–197. Available at:
1234 http://dx.doi.org/10.1016/j.gca.2015.01.026.
1235 Cameron V. and Vance D. (2014) Heavy nickel isotope compositions in rivers and the
1236 oceans. *Geochim*. *Cosmochim*. *Acta* **128**, 195–211. Available at:
1237 http://dx.doi.org/10.1016/j.gca.2013.12.007.
1238 Catts J. G. and Langmuir D. (1986) Adsorption of Cu, Pb and Zn by δMnO2:
1239 applicability of the site binding-surface complexation model. *Appl*.

Geochemistry **1**, 255–264.

Chadwick O. A., Brimhall G. H. and Hendricks D. M. (1990) From a black to a gray box—a mass balance interpretation of pedogenesis. *Geomorphology* **3**, 369–390.

Chapman J. B., Weiss D. J., Shan Y. and Lemburger M. (2009) Iron isotope fractionation during leaching of granite and basalt by hydrochloric and oxalic acids. *Geochim. Cosmochim. Acta*.

Chi Fru E., Rodríguez N. P., Partin C. A., Lalonde S. V., Andersson P., Weiss D. J., El Albani A., Rodushkin I. and Konhauser K. O. (2016) Cu isotopes in marine black shales record the Great Oxidation Event. *Proc. Natl. Acad. Sci.* **113**, 4941–4946. Available at: http://www.pnas.org/lookup/doi/10.1073/pnas.1523544113.

Coale K. H. and Bruland K. W. (1988) Copper complexation in the Northeast Pacific. *Limnol. Oceanogr.* **33**, 1084–1101.

Cornell R. M. and Giovanoli R. (1988) The influence of copper on the transformation of ferrihydrite (5Fe2O3· 9H2O) into crystalline products in alkaline media. *Polyhedron* **7**, 385–391.

Cornell R. M. and Schwertmann U. (2003) *The iron oxides: structure, properties, reactions, occurrences and uses*., John Wiley & Sons.

Coutaud A., Meheut M., Viers J., Rols J. L. and Pokrovsky O. S. (2014) Zn isotope fractionation during interaction with phototrophic biofilm. *Chem. Geol.* **390**, 46–60. Available at: http://dx.doi.org/10.1016/j.chemgeo.2014.10.004.

Coutaud M., Méheut M., Glatzel P., Pokrovski G. S., Viers J., Rols J. L. and Pokrovsky O. S. (2018) Small changes in Cu redox state and speciation generate large isotope fractionation during adsorption and incorporation of Cu by a phototrophic biofilm. *Geochim. Cosmochim. Acta* **220**, 1–18.

Dalvi A. D., Bacon W. G. and Osborne R. C. (2004) The Past and the Future of Nickel Laterites. *PDAC 2004 Int. Conv.*, 1–27.

Deer W. A., Howie R. A. and Zussman J. (1992) *An introduction to the rock-forming minerals*., Longman Scientific & Technical Hong Kong.

Dessai A. G. (2011) The geology of Goa Group: Revisited. *J. Geol. Soc. India* **78**, 233–242.

Devaraju T. C., Sudhakara T. L., Kaukonen R. J., Viljoen R. P., Alapieti T. T., Ahmed S. A. and Sivakumar S. (2010) Petrology and geochemistry of greywackes from Goa-Dharwar sector, western Dharwar craton: Implications for volcanoclastic origin. *J. Geol. Soc. India* **75**, 465–487.

Dideriksen K., Baker J. A. and Stipp S. L. S. (2008) Equilibrium Fe isotope fractionation between inorganic aqueous Fe(III) and the siderophore complex, Fe(III)-desferrioxamine B. *Earth Planet. Sci. Lett.* **269**, 280–290.

Dong S., Weiss D. J., Strekopytov S., Kreissig K., Sun Y., Baker A. R. and Formenti P. (2013) Stable isotope ratio measurements of Cu and Zn in mineral dust (bulk and size fractions) from the Taklimakan Desert and the Sahel and in aerosols from the eastern tropical North Atlantic Ocean. *Talanta* **114**, 103–109. Available at: http://dx.doi.org/10.1016/j.talanta.2013.03.062.

Doucet L. S., Laurent O., Mattielli N. and Debouge W. (2018) Zn isotope heterogeneity in the continental lithosphere: New evidence from Archean granitoids of the northern Kaapvaal craton, South Africa. *Chem. Geol.* **476**, 260–271. Available at: http://dx.doi.org/10.1016/j.chemgeo.2017.11.022.

Ehrlich S., Butler I., Halicz L., Rickard D., Oldroyd A. and Matthews A. (2004) Experimental study of the copper isotope fractionation between aqueous Cu(II) and covellite, CuS. *Chem. Geol.* **209**, 259–269.

Fernandez A. and Borrok D. M. (2009) Fractionation of Cu, Fe, and Zn isotopes during the oxidative weathering of sulfide-rich rocks. *Chem. Geol.* **264**, 1–12. Available at: http://dx.doi.org/10.1016/j.chemgeo.2009.01.024.

Frei R., Poiré D. and Frei K. M. (2014) Weathering on land and transport of chromium to the ocean in a subtropical region (Misiones, NW Argentina): A chromium stable isotope perspective. *Chem. Geol.* **381**, 110–124. Available at: http://dx.doi.org/10.1016/j.chemgeo.2014.05.015.

Fujii T. and Albarede F. (2012) Ab initio calculation of the Zn isotope effect in phosphates, citrates, and malates and applications to plants and soil. *PLoS One* **7**, 0–4.

Fujii T., Moynier F., Abe M., Nemoto K. and Albarède F. (2013) Copper isotope fractionation between aqueous compounds relevant to low temperature geochemistry and biology. *Geochim. Cosmochim. Acta* **110**, 29–44.

Fujii T., Moynier F., Blichert-Toft J. and Albarède F. (2014) Density functional theory estimation of isotope fractionation of Fe, Ni, Cu, and Zn among species relevant to geochemical and biological environments. *Geochim. Cosmochim. Acta* **140**, 553–576.

Gerth J. (1990) Unit-cell dimensions of pure and trace metal-associated goethites. *Geochim. Cosmochim. Acta* **54**, 363–371.

Goldich S. S. (1938) A Study in Rock-Weathering. *J. Geol.*

Gomez-Gonzalez M. A., Garcia-Guinea J., Laborda F. and Garrido F. (2015) Thallium occurrence and partitioning in soils and sediments affected by mining activities in Madrid province (Spain). *Sci. Total Environ.* **536**, 268–278.

Goudie A. S. (2004) Laterite. *Encycl. Geomorphol.*

Grybos M., Davranche M., Gruau G. and Petitjean P. (2007) Is trace metal release in wetland soils controlled by organic matter mobility or Fe-oxyhydroxides reduction? *J. Colloid Interface Sci.* **314**, 490–501.

Guinoiseau D., Gélabert A., Allard T., Louvat P., Moreira-Turcq P. and Benedetti M. F. (2017) Zinc and copper behaviour at the soil-river interface: New insights by Zn and Cu isotopes in the organic-rich Rio Negro basin. *Geochim. Cosmochim. Acta* **213**, 178–197. Available at: http://dx.doi.org/10.1016/j.gca.2017.06.030.

Guinoiseau D., Gélabert A., Moureau J., Louvat P. and Benedetti M. F. (2016) Zn Isotope Fractionation during Sorption onto Kaolinite. *Environ. Sci. Technol.* **50**, 1844–1852.

Harter R. D. and Naidu R. (1995) Role of metal-organic complexation in metal sorption by soils. *Adv. Agron.* **55**, 219–263.

Hayes C. T., Anderson R. F., Cheng H., Conway T. M., Edwards R. L., Fleisher M. Q., Ho P., Huang K. F., John S. G., Landing W. M., Little S. H., Lu Y., Morton P. L., Moran S. B., Robinson L. F., Shelley R. U., Shiller A. M. and Zheng X. Y. (2018) Replacement Times of a Spectrum of Elements in the North Atlantic Based on Thorium Supply. *Global Biogeochem. Cycles* **32**, 1294–1311.

Hibbert C. (2017) Controls on seasonal elemental variation in tropical rivers in Goa, India. Doctoral thesis, Birkbeck, University of London. Available at: http://bbktheses.da.ulcc.ac.uk/275/.

Hoffmann S. R., Shafer M. M. and Armstrong D. E. (2007) Strong Colloidal and Dissolved Organic Ligands Binding Copper and Zinc in Rivers. **41**, 6996–7002.

Howarth S., Prytulak J., Little S. H., Hammond S. J. and Widdowson M. (2018) Thallium concentration and thallium isotope composition of lateritic terrains. *Geochim. Cosmochim. Acta* **239**, 446–462.

Huh Y., Chan L. H., Zhang L. and Edmond J. M. (1998) Lithium and its isotopes in major world rivers: implications for weathering and the oceanic budget. *Geochim. Cosmochim. Acta* **62**, 2039–2051.

Ijichi Y., Ohno T. and Sakata S. (2018) Copper isotopic fractionation during

adsorption on manganese oxide: Effects of pH and desorption. *Geochem. J.* **52**, e1–e6.

Isson T. T., Love G. D., Dupont C. L., Reinhard C. T., Zumberge A. J., Asael D., Gueguen B., McCrow J., Gill B. C., Owens J., Rainbird R. H., Rooney A. D., Zhao M. Y., Stueeken E. E., Konhauser K. O., John S. G., Lyons T. W. and Planavsky N. J. (2018) Tracking the rise of eukaryotes to ecological dominance with zinc isotopes. *Geobiology* **16**, 341–352.

John S. G., Kunzmann M., Townsend E. J. and Rosenberg A. D. (2017) Zinc and cadmium stable isotopes in the geological record: A case study from the post-snowball Earth Nuccaleena cap dolostone. *Palaeogeogr. Palaeoclimatol. Palaeoecol.* **466**, 202–208. Available at: http://dx.doi.org/10.1016/j.palaeo.2016.11.003.

Jouvin D., Louvat P., Juillot F., Maréchal C. N. and Benedetti M. F. (2009) Zinc isotopic fractionation: Why organic matters. *Environ. Sci. Technol.* **43**, 5747–5754.

Juillot F., Maréchal C., Ponthieu M., Cacaly S., Morin G., Benedetti M., Hazemann J. L., Proux O. and Guyot F. (2008) Zn isotopic fractionation caused by sorption on goethite and 2-Lines ferrihydrite. *Geochim. Cosmochim. Acta* **72**, 4886–4900.

Kimball B. E., Mathur R., Dohnalkova A. C., Wall A. J., Runkel R. L. and Brantley S. L. (2009) Copper isotope fractionation in acid mine drainage. *Geochim. Cosmochim. Acta* **73**, 1247–1263. Available at: http://dx.doi.org/10.1016/j.gca.2008.11.035.

Koschinsky A. and Hein J. R. (2003) Uptake of elements from seawater by ferromanganese crusts: Solid-phase associations and seawater speciation. *Mar. Geol.* **198**, 331–351.

Kump L. R., Brantley S. L. and Arthur M. A. (2000) Chemical Weathering, Atomospheric CO2, and Climate. *Annu. Rev. Earth Planet. Sci.* **28**, 611–667.

Kunzmann M., Halverson G. P., Sossi P. A., Raub T. D., Payne J. L. and Kirby J. (2013) Zn isotope evidence for immediate resumption of primary productivity after snowball Earth. *Geology* **41**, 27–30.

Larner F. and Rehkämper M. (2012) Evaluation of Stable Isotope Tracing for ZnO Nanomaterials · New Constraints from High Precision Isotope Analyses and Modeling. *Environ. Sci. Technol.* **46**, 4149–4158.

Larner F., Rehkämper M., Coles B. J., Kreissig K., Weiss D. J., Sampson B., Unsworth C. and Strekopytov S. (2011) A new separation procedure for Cu prior to stable isotope analysis by MC-ICP-MS. *J. Anal. At. Spectrom.* **26**, 1627–1632.

Lebedeva M. I., Fletcher R. C. and Brantley S. L. (2010) A mathematical model for steady-state regolith production at constant erosion rate. *Earth Surf. Process. Landforms* **35**, 508–524.

Little S. H., Sherman D. M., Vance D. and Hein J. R. (2014a) Molecular controls on Cu and Zn isotopic fractionation in Fe-Mn crusts. *Earth Planet. Sci. Lett.* **396**, 213–222.

Little S. H., Vance D., Walker-Brown C. and Landing W. M. (2014b) The oceanic mass balance of copper and zinc isotopes, investigated by analysis of their inputs, and outputs to ferromanganese oxide sediments. *Geochim. Cosmochim. Acta* **125**, 673–693.

Liu S. A., Teng F. Z., Li S., Wei G. J., Ma J. L. and Li D. (2014) Copper and iron isotope fractionation during weathering and pedogenesis: Insights from saprolite profiles. *Geochim. Cosmochim. Acta* **146**, 59–75. Available at: http://dx.doi.org/10.1016/j.gca.2014.09.040.

Lupker M., France-Lanord C., Lavé J., Bouchez J., Galy V., Métivier F., Gaillardet J., Lartiges B. and Mugnier J. L. (2011) A Rouse-based method to integrate the chemical composition of river sediments: Application to the Ganga basin. *J. Geophys. Res. Earth Surf.* **116**, 1–24.

Lv Y., Liu S. A., Zhu J. M. and Li S. (2016) Copper and zinc isotope fractionation during deposition and weathering of highly metalliferous black shales in central China. *Chem. Geol.* **445**, 24–35. Available at: http://dx.doi.org/10.1016/j.chemgeo.2016.01.016.

Manceau a, Schlegel M. ., Musso M., Sole V. ., Gauthier C., Petit P. . and Trolard F. (2000) Crystal chemistry of trace elements in natural and synthetic goethite. *Geochim. Cosmochim. Acta* **64**, 3643–3661.

Manceau A., Lanson B. and Drits V. A. (2002) Structure of heavy metal sorbed birnessite. Part III: Results from powder and polarized extended X-ray absorption fine structure spectroscopy. *Geochim. Cosmochim. Acta* **66**, 2639–2663.

Maréchal C. and Albarède F. (2002) Ion-exchange fractionation of copper and zinc isotopes. *Geochim. Cosmochim. Acta* **66**, 1499–1509.

1409 Maréchal C. N., Télouk P. and Albarède F. (1999) Precise analysis of copper and zinc
1410 isotopic compositions by plasma-source mass spectrometry. *Chem*. *Geol*. **156**,
1411 251–273.
1412 Marković T., Manzoor S., Humphreys-Williams E., Kirk G. J. D., Vilar R. and Weiss
1413 D. J. (2017) Experimental Determination of Zinc Isotope Fractionation in
1414 Complexes with the Phytosiderophore 2′-Deoxymugeneic Acid (DMA) and Its
1415 Structural Analogues, and Implications for Plant Uptake Mechanisms. *Environ*.
1416 *Sci*. *Technol*. **51**, 98–107.
1417 Mathur R., Jin L., Prush V., Paul J., Ebersole C., Fornadel A., Williams J. Z. and
1418 Brantley S. (2012) Cu isotopes and concentrations during weathering of black
1419 shale of the Marcellus Formation, Huntingdon County, Pennsylvania (USA).
1420 *Chem*. *Geol*. **304**–**305**, 175–184. Available at:
1421 http://dx.doi.org/10.1016/j.chemgeo.2012.02.015.
1422 Mathur R., Ruiz J., Titley S., Liermann L., Buss H. and Brantley S. (2005) Cu
1423 isotopic fractionation in the supergene environment with and without bacteria.
1424 *Geochim*. *Cosmochim*. *Acta* **69**, 5233–5246.
1425 McBride M. B. (1981) Forms and distribution of copper in solid and solution phases
1426 of soil. In *Copper in Soils and Plants* (eds. J. F. Loneragan, A. D. Robson, and
1427 R. D. Graham). Academic Press: Australia.
1428 McBride M., Sauvé S., Hendershot W., Sauve S. and Hendershot W. (1997)
1429 Solubility control of Cu, Zn, Cd and Pb in contaminated soils. *Eur*. *J*. *Soil Sci*.
1430 **48**, 337–346.
1431 McFarlane M. J. (1983) Laterites. In *Chemical sediments and geomorphology*
1432 McFarlane M. J. (1976) Morphological mapping in laterite areas. *Stud*. *Geogr*. *Brno*.
1433 Moeller K., Schoenberg R., Pedersen R. B., Weiss D. and Dong S. (2012) Calibration
1434 of the New Certified Reference Materials ERM-AE633 and ERM-AE647 for
1435 Copper and IRMM-3702 for Zinc Isotope Amount Ratio Determinations.
1436 *Geostand*. *Geoanalytical Res*. **36**, 177–199.
1437 Moffett J. W. and Brand L. E. (1996) Production of strong, extracellular Cu chelators
1438 by marine cyanobacteria in response to Cu stress. *Limnol*. *Oceanogr*. **41**, 388–
1439 395.
1440 Morgan J. L. L., Wasylenki L. E., Nuester J. and Anbar A. D. (2010) Fe isotope
1441 fractionation during equilibration of Fe-organic complexes. *Environ*. *Sci*.
1442 *Technol*. **44**, 6095–6101.

1443 Moynier F., Vance D., Fujii T. and Savage P. (2017) The Isotope Geochemistry of
1444 Zinc and Copper. *Rev*. *Mineral*. *Geochemistry* **82**, 543–600. Available at:
1445 http://rimg.geoscienceworld.org/lookup/doi/10.2138/rmg.2017.82.13.
1446 Neaman A., Chorover J. and Brantley S. L. (2005a) Element mobility patterns record
1447 organic ligands in soils on early Earth. *Geology* **33**, 117–120.
1448 Neaman A., Chorover J. and Brantley S. L. (2005b) Implications of the evolution of
1449 organic acid moieties for basalt weathering over geological time. *Am*. *J*. *Sci*. **305**,
1450 147–185.
1451 Nesbitt H. W. and Young G. M. (1982) Early proterozoic climates and plate motions
1452 inferred from major element chemistry of lutites. *Nature*.
1453 Neubert N., Heri A. R., Voegelin A. R., Nägler T. F., Schlunegger F. and Villa I. M.
1454 (2011) The molybdenum isotopic composition in river water: Constraints from
1455 small catchments. *Earth Planet*. *Sci*. *Lett*. **304**, 180–190. Available at:
1456 http://dx.doi.org/10.1016/j.epsl.2011.02.001.
1457 Newbold T. J. (1844) Notes chiefly geological, across the Peninsula from
1458 Masultipatam to Goa, comprising remarks on the origin of regur and laterite:
1459 Occurrence of manganese veins in the latter and on certain traces of aqueous
1460 denudation on the surface of southern India. *J*. *Asiat*. *Soc*. *Beng*. **15**, 204–213.
1461 Nielsen S. G., Rehkämper M., Baker J. and Halliday A. N. (2004) The precise and
1462 accurate determination of thallium isotope compositions and concentrations for
1463 water samples by MC-ICPMS. *Chem*. *Geol*. **204**, 109–124.
1464 Opfergelt S., Cornélis J. T., Houben D., Givron C., Burton K. W. and Mattielli N.
1465 (2017) The influence of weathering and soil organic matter on Zn isotopes in
1466 soils. *Chem*. *Geol*. **466**, 140–148. Available at:
1467 http://dx.doi.org/10.1016/j.chemgeo.2017.06.002.
1468 Pascoe K. H. (1950) *A manual of the geology of India and Burma, Vol*. *1*., Govt of
1469 India, New Dehli.
1470 Paton C., Hergt J. M., Phillips D., Woodhead J. D. and Shee S. R. (2007) New
1471 insights into the genesis of Indian kimberlites from the Dharwar Craton via in
1472 situ Sr isotope analysis of groundmass perovskite. *Geology* **35**, 1011–1014.
1473 Peacock C. L. and Sherman D. M. (2007) Sorption of Ni by birnessite: Equilibrium
1474 controls on Ni in seawater. *Chem*. *Geol*. **238**, 94–106.
1475 Pokrovsky O. S., Viers J., Emnova E. E., Kompantseva E. I. and Freydier R. (2008)
1476 Copper isotope fractionation during its interaction with soil and aquatic

microorganisms and metal oxy(hydr)oxides: Possible structural control. *Geochim. Cosmochim. Acta* **72**, 1742–1757.

Pokrovsky O. S., Viers J. and Freydier R. (2005) Zinc stable isotope fractionation during its adsorption on oxides and hydroxides. *J. Colloid Interface Sci.* **291**, 192–200.

Pons M. L., Fujii T., Rosing M., Quitté G., Télouk P. and Albarède F. (2013) A Zn isotope perspective on the rise of continents. *Geobiology* **11**, 201–214.

Post J. E. (1999) Manganese oxide minerals: Crystal structures and economic and environmental significance. *Proc. Natl. Acad. Sci.*

Roser B. P., Cooper R. A., Nathan S. and Tulloch A. J. (1996) Reconnaissance sandstone geochemistry, provenance, and tectonic setting of the lower Paleozoic terranes of the West Coast and Nelson, New Zealand. *New Zeal. J. Geol. Geophys.*

Ross S. J., Franzmeier D. P. and Roth C. B. (1976) Mineralogy and chemistry of manganese oxides in some Indiana soils. *Soil Sci. Soc. Am. J.* **40**, 137–143.

Ryan B. M., Kirby J. K., Degryse F., Scheiderich K. and McLaughlin M. J. (2014) Copper isotope fractionation during equilibration with natural and synthetic ligands. *Environ. Sci. Technol.* **48**, 8620–8626.

Schellman W. (1983) Geochemical principles of lateritic nickel ore formation. *Proc. Int. Semin. Lateritisation Process.*, 119–135. Available at: http://ci.nii.ac.jp/naid/10003418711/en/ [Accessed October 23, 2018].

Schmidt P. W., Prasad V. and Ramam P. K. (1983) Magnetic ages of some Indian laterites. *Palaeogeogr. Palaeoclimatol. Palaeoecol.* **44**, 185–202. Available at: https://www.sciencedirect.com/science/article/pii/0031018283901025 [Accessed January 24, 2018].

Schnoor J. L. (1990) Kinetics of chemical weathering: a comparison of laboratory and field weathering rates. In *Aquatic Chemical Kinetics: Reaction Rates of Processes in Natural Waters* (ed. W. Stumm). Zurich: Swiss Fed. Inst. Technol. pp. 475–504.

Shank G. C., Skrabal S. A., Whitehead R. F. and Kieber R. J. (2004) Strong copper complexation in an organic-rich estuary: the importance of allochthonous dissolved organic matter. *Mar. Chem.* **88**, 21–39.

Sherman D. M. (2013) Equilibrium isotopic fractionation of copper during oxidation/reduction, aqueous complexation and ore-forming processes:

Predictions from hybrid density functional theory. *Geochim*. *Cosmochim*. *Acta* **118**, 85–97. Available at: http://dx.doi.org/10.1016/j.gca.2013.04.030.

Sherman D. M. and Peacock C. L. (2010) Surface complexation of Cu on birnessite (δ-MnO2): Controls on Cu in the deep ocean. *Geochim*. *Cosmochim*. *Acta* **74**, 6721–6730. Available at: http://dx.doi.org/10.1016/j.gca.2010.08.042.

Siebert C., Nagler T. F. and Kramers J. D. (2001) Determination of molybdenum isotope fractionation by double-spike multicollector inductively coupled plasma mass spectrometry. *Geochemistry*, *Geophys*. *Geosystems* **2**, 1032.

Singh B. and Gilkes R. J. (1992) Properties and distribution of iron oxides and their association with minor elements in the soils of south- western Australia. *Eur*. *J*. *Soil Sci*. **43**, 77–98.

Srinivasan R., Naqvi S. M., Raj B. U., Rao D. V. S., Balaram V. and Rao T. G. (1989) Geochemistry of the Archaean greywackes from the northwestern part of the Chitradurga schist belt, Dharwar Craton, South India-evidence for granitoid upper crust in the Archaean. *Geol*. *Soc*. *India* **34**, 505–516.

Stevenson E. I., Fantle M. S., Das S. B., Williams H. M. and Aciego S. M. (2017) The iron isotopic composition of subglacial streams draining the Greenland ice sheet. *Geochim*. *Cosmochim*. *Acta* **213**, 237–254. Available at: http://dx.doi.org/10.1016/j.gca.2017.06.002.

Suhr N., Schoenberg R., Chew D., Rosca C., Widdowson M. and Kamber B. S. (2018) Elemental and isotopic behaviour of Zn in Deccan basalt weathering profiles: Chemical weathering from bedrock to laterite and links to Zn deficiency in tropical soils. *Sci*. *Total Environ*. **619–620**, 1451–1463. Available at: https://doi.org/10.1016/j.scitotenv.2017.11.112.

Swoboda-Colberg N. G. and Drever J. I. (1993) Mineral dissolution rates in plot-scale field and laboratory experiments. *Chem*. *Geol*. **105**, 51–69.

Szynkiewicz A. and Borrok D. M. (2016) Isotope variations of dissolved Zn in the Rio Grande watershed, USA: The role of adsorption on Zn isotope composition. *Earth Planet*. *Sci*. *Lett*. **433**, 293–302.

Tardy Y. (1997) *Petrology of laterites and tropical soils*., A.A. Balkema, Rotterdam. Available at: https://www.cabdirect.org/cabdirect/abstract/19981913040.

Tardy Y., Kobilsek B. and Paquet H. (1991) Mineralogical composition and geographical distribution of African and Brazilian periatlantic laterites. The influence of continental drift and tropical paleoclimates during the past 150

million years and implications for India and Australia. *J. African Earth Sci. (and Middle East)* **12**, 283–295.

Taylor G. and Eggleton R. A. (2001) *Regolith Geology and Geomorphology*., John Wiley & Sons.

Taylor R. M., McKenzie R. M. and Norrish K. (1964) The mineralogy and chemistry of manganese in some australian soils. *Aust. J. Soil Res.* **2**, 235–248.

Telus M., Dauphas N., Moynier F., Tissot F. L. H., Teng F.-Z., Nabelek P. I., Craddock P. R. and Groat L. A. (2012) Iron, zinc, magnesium and uranium isotopic fractionation during continental crust differentiation: The tale from migmatites, granitoids, and pegmatites. *Geochim. Cosmochim. Acta* **97**, 247–265.

Tessier A., Fortin D., Belzile N., DeVitre R. R. and Leppard G. G. (1996) Metal sorption to diagenetic iron and manganese oxyhydroxides and associated organic matter: Narrowing the gap between field and laboratory measurements. *Geochim. Cosmochim. Acta* **60**, 387–404.

Thorne R. L., Roberts S. and Herrington R. (2012) Climate change and the formation of nickel laterite deposits. *Geology* **40**, 331–334.

Tokashiki Y., Dlxon J. B. and Golden D. C. (1986) Manganese Oxide Analysis in Soils by Combined X-ray Diffraction and Selective Dissolution Methods 1. *Soil Sci. Soc. Am. J.*

Uzochukwu G. A. and Dixon J. B. (1986) Manganese oxide minerals in nodules of two soils of Texas and Alabama. *Soil Sci. Soc. Am. J.* **50**, 1358–1363.

Vance D., Archer C., Bermin J., Perkins J., Statham P. J., Lohan M. C., Ellwood M. J. and Mills R. A. (2008) The copper isotope geochemistry of rivers and the oceans. *Earth Planet. Sci. Lett.* **274**, 204–213.

Vance D., Matthews A., Keech A., Archer C., Hudson G., Pett-Ridge J. and Chadwick O. A. (2016) The behaviour of Cu and Zn isotopes during soil development: Controls on the dissolved load of rivers. *Chem. Geol.* **445**, 36–53. Available at: http://dx.doi.org/10.1016/j.chemgeo.2016.06.002.

Vdović N., Bišćan J. and Juračić M. (1991) Relationship between specific surface area and some chemical and physical properties of particulates: study in the northern Adriatic. *Mar. Chem.* **36**, 317–328.

Viers J., Oliva P., Nonell A., Gélabert A., Sonke J. E., Freydier R., Gainville R. and Dupré B. (2007) Evidence of Zn isotopic fractionation in a soil-plant system of a

pristine tropical watershed (Nsimi, Cameroon). *Chem. Geol.* **239**, 124–137.

Weiss D. J., Boye K., Caldelas C. and Fendorf S. (2014) Zinc Isotope Fractionation during Early Dissolution of Biotite Granite. *Soil Sci. Soc. Am. J.* **78**, 171. Available at: https://www.soils.org/publications/sssaj/abstracts/78/1/171.

Weiss D. J., Rausch N., Mason T. F. D., Coles B. J., Wilkinson J. J., Ukonmaanaho L., Arnold T. and Nieminen T. M. (2007) Atmospheric deposition and isotope biogeochemistry of zinc in ombrotrophic peat. *Geochim. Cosmochim. Acta* **71**, 3498–3517.

Welch S. A. and Ullman W. J. (1996) Feldspar dissolution in acidic and organic solutions: Compositional and pH dependence of dissolution rate. *Geochim. Cosmochim. Acta*.

Welch S. A. and Ullman W. J. (1993) The effect of organic acids on plagioclase dissolution rates and stoichiometry. *Geochim. Cosmochim. Acta*.

Welch S. A. and Ullman W. J. (2000) The temperature dependence of bytownite feldspar dissolution in neutral aqueous solutions of inorganic and organic ligands at low temperature (5-35°C). *Chem. Geol.*

Wells M. L., Kozelka P. B. and Bruland K. W. (1998) The complexation of "dissolved" Cu, Zn, Cd and Pb by soluble and colloidal organic matter in Narragansett Bay, RI. *Mar. Chem.* **62**, 203–217.

West A. J., Galy A. and Bickle M. (2005) Tectonic and climatic controls on silicate weathering. *Earth Planet. Sci. Lett.* **235**, 211–228.

White A. F. and Buss H. L. (2014) Natural Weathering Rates of Silicate Minerals. *Treatise on Geochemistry*, 115–155. Available at: https://www.sciencedirect.com/science/article/pii/B9780080959757005040?via%3Dihub [Accessed November 16, 2018].

Widdowson M. (2009) *Evolution of Laterite in Goa.*, Available at: http://oro.open.ac.uk/19793/.

Widdowson M. (2004) Ferricrete, Ferralitisation. In *Encyclopedia of Geomorphology* (ed. A. S. Goudie). Routledge, London. pp. 365–367.

Widdowson M. (2007) Laterite and Ferricrete. In *Geochemical Sediments and Landscapes* (eds. D. J. Nash and S. J. McLaren). Blackwell Publishing Ltd. pp. 46–94.

Widdowson M. (1997) Tertiary palaeosurfaces of the SW Deccan, Western India: implications for passive margin uplift. *Geol. Soc. London, Spec. Publ.* **120**, 221–

248. Available at: http://sp.lyellcollection.org/lookup/doi/10.1144/GSL.SP.1997.120.01.15.

Widdowson M. and Gunnell Y. (1999) *Lateritization, Geomorphology and Geodynamics of a Passive Continental Margin: The Konkan and Kanara Coastal Lowlands of Western Peninsular India*.,

Wiederhold J. G., Kraemer S. M., Teutsch N., Borer P. M., Halliday A. N. and Kretzschmar R. (2006) Iron isotope fractionation during proton-promoted, ligand-controlled, and reductive dissolution of goethite. *Environ*. *Sci*. *Technol*. **40**, 3787–3793.

Wimpenny J., Gannoun A., Burton K. W., Widdowson M., James R. H. and Gíslason S. R. (2007) Rhenium and osmium isotope and elemental behaviour accompanying laterite formation in the Deccan region of India. *Earth Planet*. *Sci*. *Lett*. **261**, 239–258.

Xue H. Bin, Kistler D. and Sigg L. (1995) Competition of copper and zinc for strong ligands in a eutrophic lake. *Limnol*. *Oceanogr*. **40**, 1142–1152.

Table 1

Table 1. Isotope data for USGS rock standards (mean and 2SD) analysed in this study (in grey) versus recommended (Moynier et al., 2017) or published values.

	$\delta^{66}Zn_{JMC\text{-}Lyon}$ (‰)	2SD	n	$\delta^{65}Cu_{SRM976}$ (‰)	2SD	n
BHVO-2	0.39	0.07	6	0.07	0.05	6
Recommended	*0.28*			*0.12*		
Published Range	*0.21 to 0.48*		*7*	*0.10 to 0.15*		*5*
BIR-1	0.27	0.04	3	-0.02	0.05	3
Recommended	*0.26*			*0.02*		
Published Range	*0.20 to 0.36*		*5*	*-0.02 to 0.08*		*3*
Nod P1	0.86	0.06	3	0.28	0.09	3
Published Range	*0.78 to 0.87*		*3*	*0.29 to 0.46*		*3*
BCR-2	0.33	0.06	3	nd		
*Recommended**	*0.25*			*0.17*		
*Published Range**	*0.20 to 0.33*		*12*	*0.07 to 0.22*		*6*

* Combined BCR1/2

'n' refers to the number of complete duplicates analysed in this study, or the number of studies compiled in the given published range.

Table 2

Table 2. Data table, including calculated CIA and IOL values (see text for details), S concentrations, calculated τ values (where j = Nb, and p = SQ2-6 mean: see Eqn. 5 and text for details), measured Zn and Cu isotope values, and calculated Δ isotope values (where $\Delta = \delta_{sample} - \delta_{SQ2}$). Fe_2O_3 and MnO concentrations from Wimpenny et al. (2007). Li, Zn and Cu concentrations from Howarth et al. (2018).

Zone	Sample	Depth m	ρ gcm^{-3}	CIA	IOL	S µg/g	Fe_2O_3 wt%	MnO wt%	Li µg/g	Zn µg/g	Cu µg/g	$\tau_{Fe,Nb}$	$\tau_{Mn,Nb}$	$\tau_{Li,Nb}$	$\tau_{Zn,Nb}$	$\tau_{Cu,Nb}$	$\delta^{66}Zn$ ‰	2 SD	$\Delta^{66}Zn$ ‰	$\delta^{65}Cu$ ‰	2 SD	$\Delta^{65}Cu$ ‰
	SQ14	0	1.45	97	86	350	48.5	0.04	8.8	31	61	2.7	-0.89	-0.88	-0.87	-0.52	-0.02	0.07	-0.51	-0.87	0.07	-0.89
IV	SQ13	2.5	1.57	97	82	418	45.0	0.04	9.5	25	50	2.9	-0.87	-0.85	-0.89	-0.56	nd	nd	na	-0.70	0.07	-0.73
	SQ12	3.5	1.64	98	80	274	36.4	0.06	7.1	25	39	1.6	-0.85	-0.91	-0.90	-0.71	0.07	0.07	-0.42	-0.69	0.07	-0.67
	SQ12dup																nd			-0.61	0.07	
III	SQ11	7.5	1.25	95	84	203	68.3	0.57	4.2	97	52	18.9	5.5	-0.78	0.51	0.54	0.14	0.07	-0.34	-0.30	0.07	-0.32
	SQ10	8.5	1.80	96	82	408	49.6	0.02	4.5	21	31	4.6	-0.91	-0.91	-0.87	-0.64	0.15	0.07	-0.33	-0.86	0.07	-0.89
	SQ9	12	1.29	92	31	205	10.8	0.02	8.7	23	34	0.59	-0.91	-0.77	-0.82	-0.49	0.28	0.07	-0.20	-0.60	0.07	-0.63
II	SQ8	13.5	1.37	92	31	227	10.3	0.02	9.7	38	38	0.37	-0.87	-0.77	-0.73	-0.48	0.02	0.07	-0.46	-0.45	0.07	-0.47
	SQ7	14	1.25	90	27	192	7.6	0.06	13.8	38	42	0.07	-0.64	-0.66	-0.72	-0.40	0.38	0.07	-0.11	-0.03	0.07	-0.06
	SQ6	15	2.20	59	18	630	3.4	0.05	20.2	66	53	-0.26	-0.46	-0.22	-0.23	0.19	0.42	0.07	-0.06	-0.23	0.07	-0.25
	SQ5	22.5	1.99	63	27	861	7.6	0.17	45.0	146	37	0.44	0.59	0.51	0.47	-0.29	0.53	0.07	0.05	-0.28	0.07	-0.31
I	SQ4	25.5	2.23	57	15	343	2.4	0.07	12.5	33	66	-0.20	0.01	-0.27	-0.43	1.24	0.43	0.07	-0.05	-0.05	0.07	-0.08
	SQ3	30	2.68	58	22	818	5.6	0.11	32.4	115	40	-0.12	-0.22	-0.10	-0.04	-0.36	0.47	0.07	-0.01	0.04	0.07	0.02
	SQ2	34	2.75	57	23	725	6.1	0.13	31.6	112	50	0.04	0.06	-0.04	0.02	-0.12	0.51	0.07	na	0.01	0.07	na
	SQ2dup																0.48	0.07		0.04	0.07	
Dyke	SQ1	-	3.11	-	-	1634	-	-	7.4	127	122			na	na	na	0.35	0.07	na	0.08	0.07	na
											Integrated (all):	**1.5**	**0.02**	**-0.28**	**-0.23**	**-0.07**			**-0.14**			**-0.32**
											Integrated (excl. zone III):	**0.36**	**-0.21**	**-0.21**	**-0.22**	**-0.06**			**-0.11**			**-0.28**

nd – not done
na – not applicable

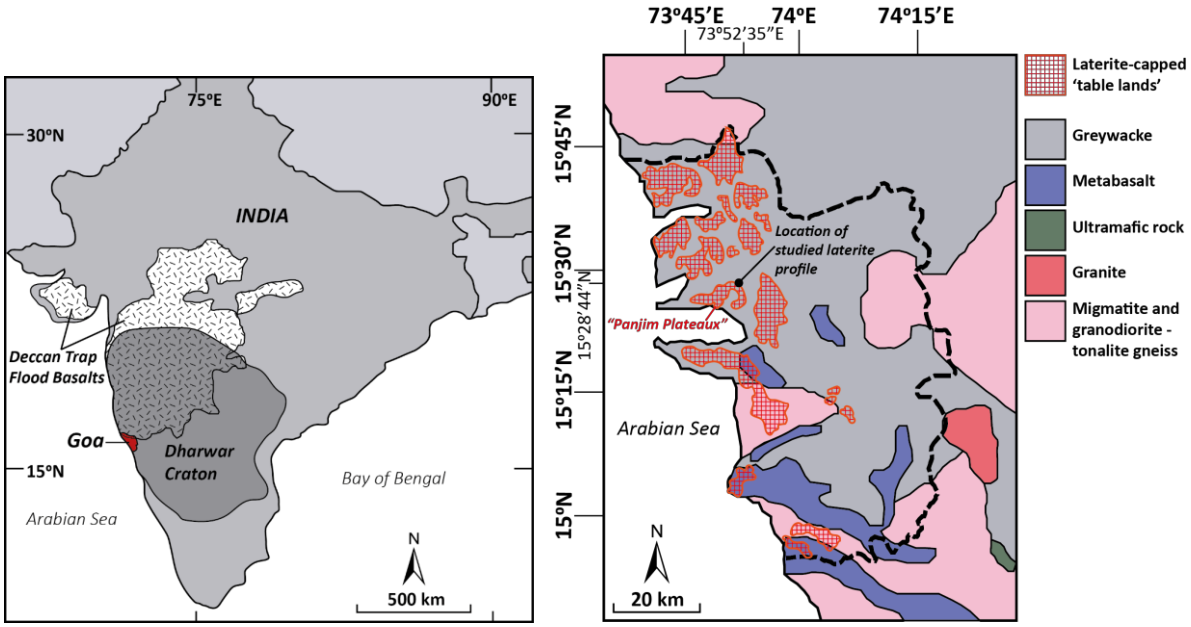

Figure 1. **Left**: The location of Goa state (red) on the Indian Dharwar Craton (adapted from Paton et al., 2007). In the northeastern corner of the state, Deccan Trap flood basalts overlie the Dharwar metasediments. **Right**: The geology of Goa state (adapted from Devaraju et al., 2010 and Widdowson, 2009). The black dashed line represents the state boundary. The Merces Quarry (SQ) laterite profile (labelled) is located at 15°28'44"N, 73°52'35"E. It is developed on Dharwar Late Archaean biotite-bearing greywacke.

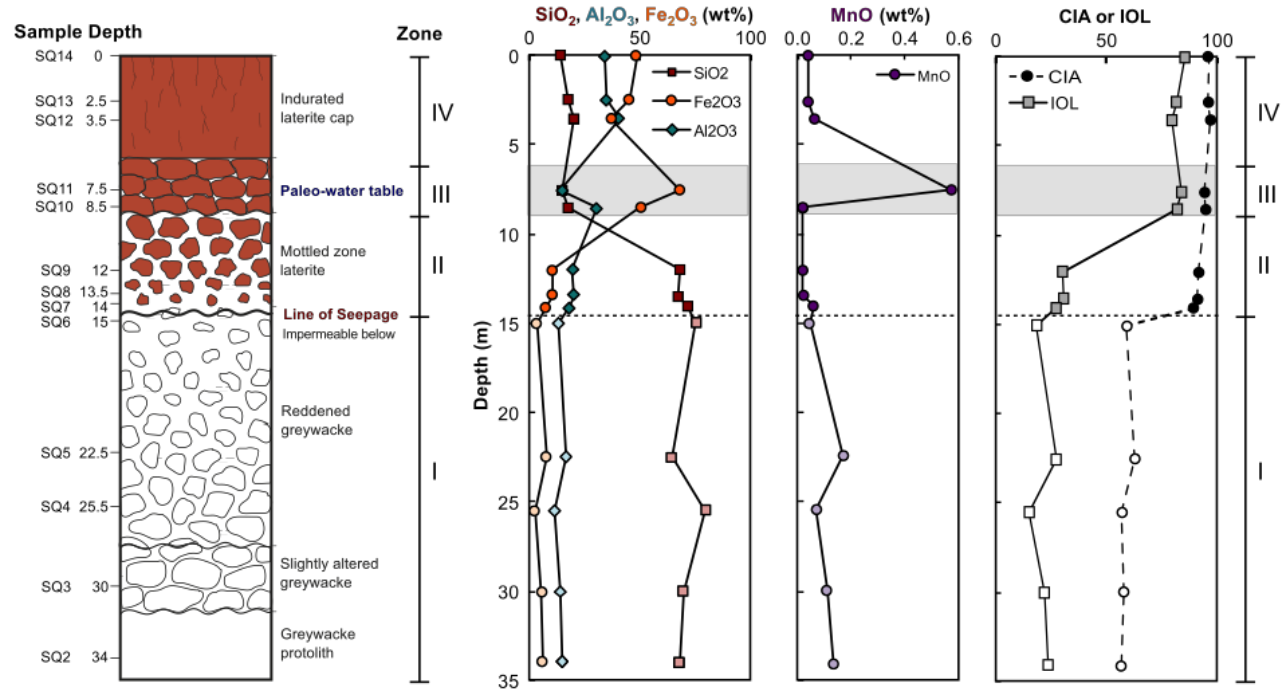

Figure 2. Left: Schematic illustrating the depth distribution of samples in the laterite profile in relation to characteristic zones of alteration (Wimpenny et al., 2007; Widdowson, 2009). Graphs from left to right: Major element concentration variations (SiO_2, Al_2O_3, Fe_2O_3; Widdowson, 2009), MnO concentration variations (Widdowson, 2009), and indices of alteration (Chemical Index of Alteration, CIA; Index of Lateritization, IOL; see text for further details). Grey shading highlights zone III, the paleo-water table. Samples showing only limited alteration, from below the dotted line of seepage (zone I), are paler in colour.

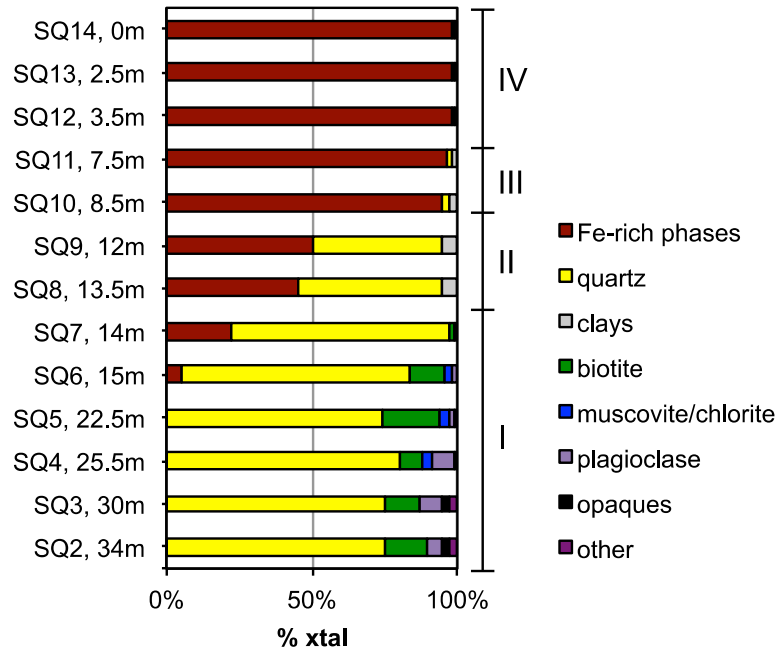

Figure 3. The crystal abundances of major mineral phases in the SQ laterite weathering profile compared to the four identified zones of alteration (see also Fig. 2; after Wimpenney et al., 2007).

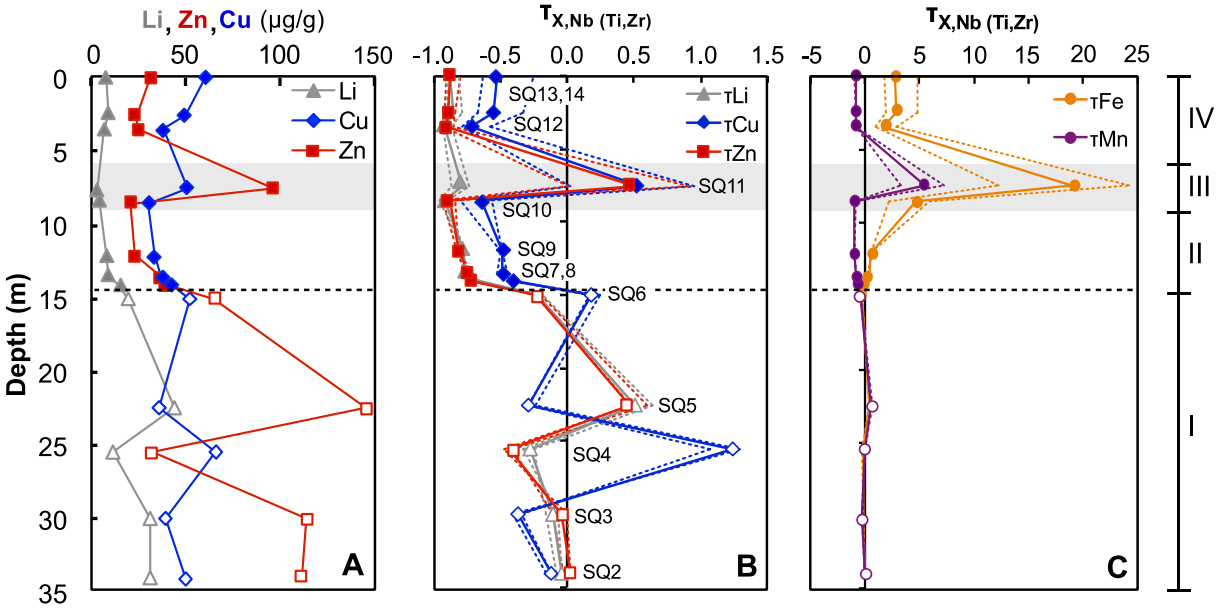

Figure 4. A. Concentration profiles and **B.** τ enrichment-depletion profiles (see text for details) of Li (grey triangles), Zn (red squares) and Cu (blue diamonds) in the SQ profile. **C**. τ enrichment-depletion profiles for Fe and Mn. Open symbols: little altered samples in zone I, below line of seepage (dotted line). Filled symbols: altered samples in zones II-IV, above line of seepage. Grey shaded zone III has been influenced by the paleo-water table.

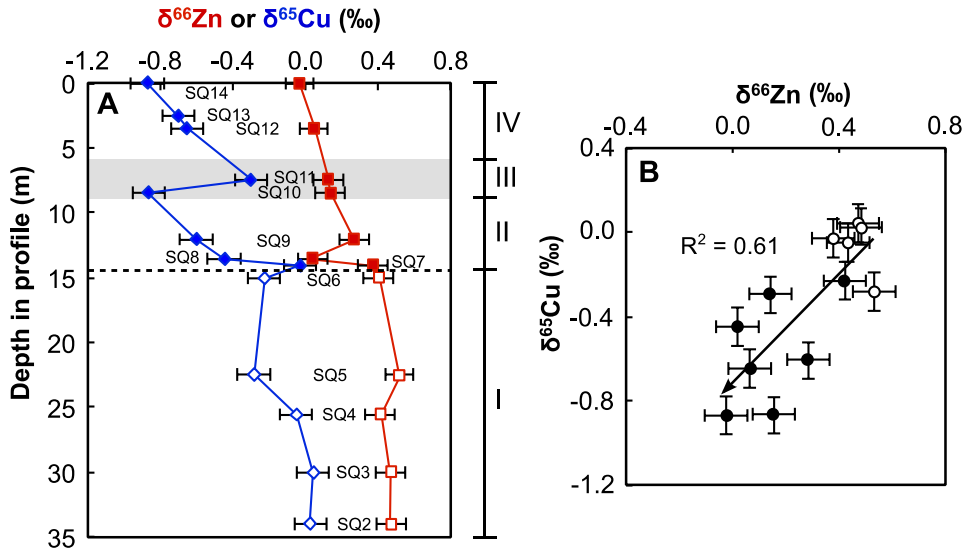

Figure 5. A. Depth profiles of δ^{66}Zn (red squares) and δ^{65}Cu (blue diamonds). Open symbols: unaltered-little altered samples in zone I, below line of seepage (dotted line). Filled symbols: increasingly altered zone II-IV mottled and lateritic samples. Shaded grey rectangle: zone III, influenced by the paleo-water table. **B**. Positive correlation between δ^{66}Zn and δ^{65}Cu in the SQ profile. Linear regression (arrow) indicates coupled loss of heavy Cu and Zn isotopes during lateritization and a resultant shift towards residual isotopically light values. Error bars represent long-term external 2SD reproducibility.

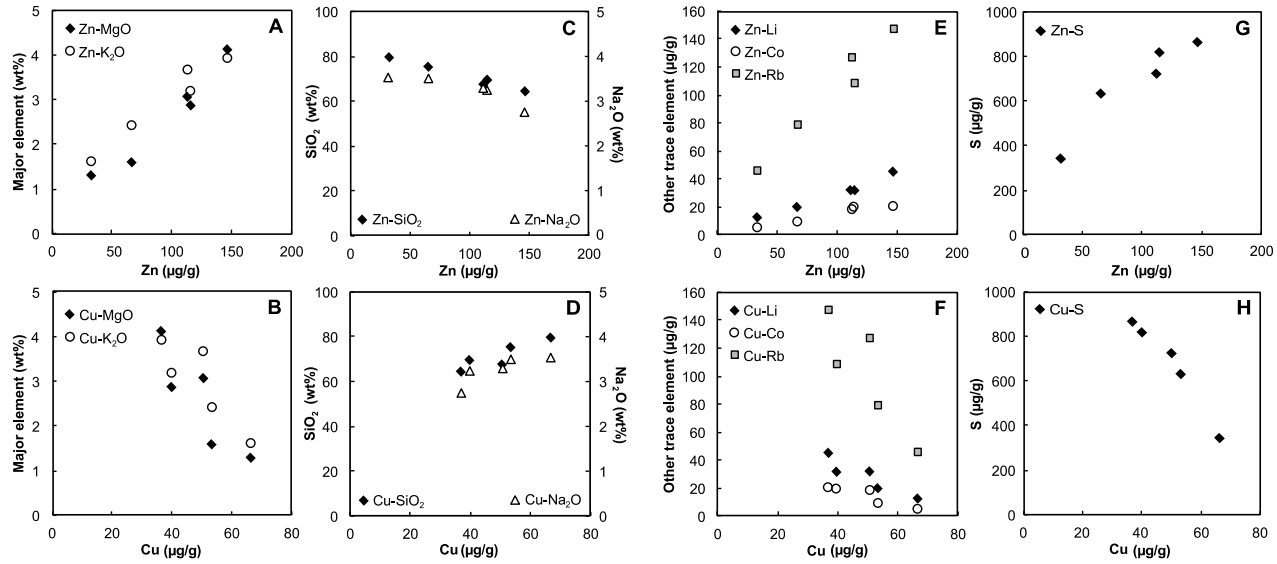

Figure 6. Covariation of Zn and Cu with selected major (A-D) and trace elements (E-H) in samples from zone I (unaltered – little altered) of the SQ laterite profile. Positive correlations of Zn with elements commonly hosted in biotite (Mg, K, Li, Co and Rb) suggest that Zn is primarily hosted in biotite in the parent greywacke (see also Fig. S3). Copper shows negative correlations with most other major and trace elements, with the exception of SiO_2 and Na_2O (Panel D), suggesting an association with a detrital phase.

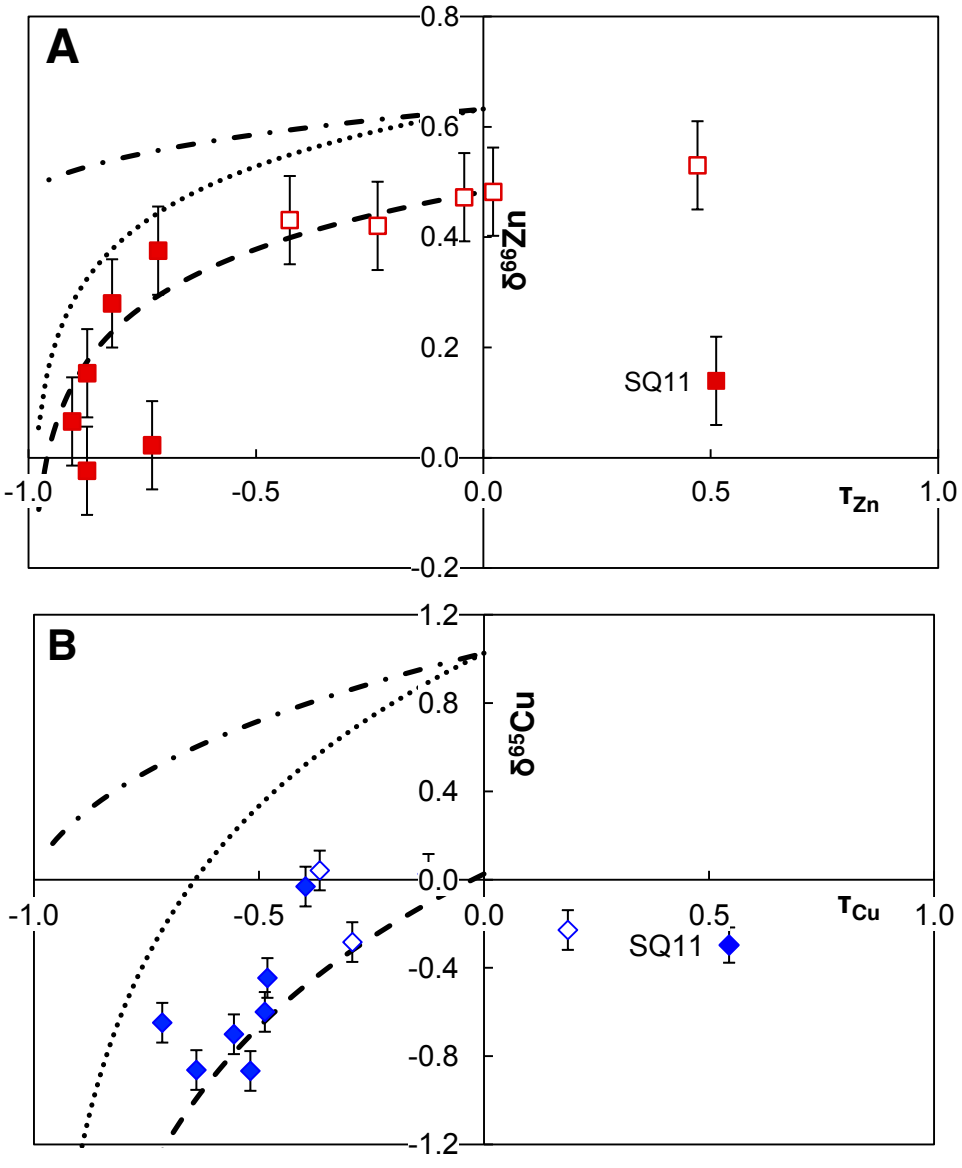

4C)

Figure 7. Rayleigh fractionation modelling of **A**. Zn and **B**. Cu isotopes assuming preferential mobilization of heavy isotopes to the dissolved phase, assuming $R = R_0 . f^{\alpha - 1}$ (where R_0 is the isotope ratio of the protolith (larger open symbols), f the fraction removed and α the fractionation factor. For Zn: α = 1.00015, for Cu: α = 1.001). Dashed line: residual isotopic composition of the solid. Dash-dotted line: cumulative isotopic composition of the fluid removed from the system. Dotted line: instantaneous fluid isotopic composition. Symbols as in Figures 4 and 5. Error bars represent long-term external 2SD reproducibility. Paleo-water table sample SQ11 labelled.

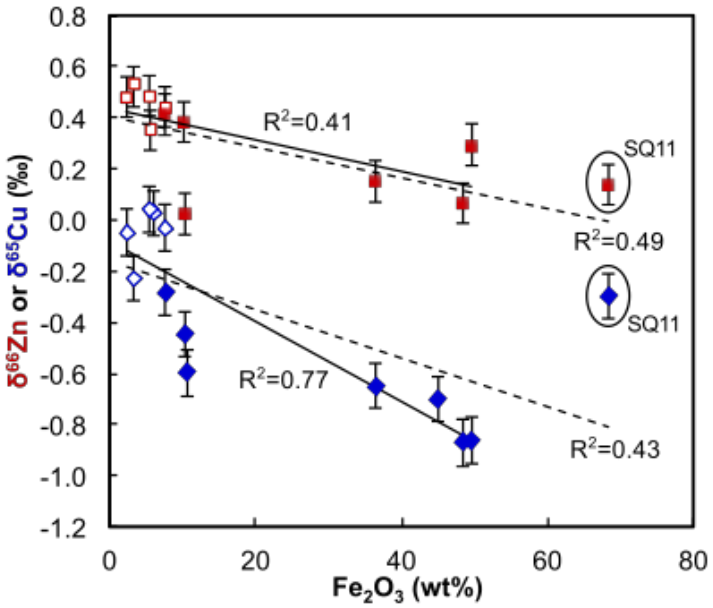

Figure 8. Negative correlations of $\delta^{66}Zn$ (red squares) and $\delta^{65}Cu$ (blue diamonds) with Fe_2O_3 in the SQ profile. Paleo-water table sample SQ11 is circled, other symbols as in Figure 5. Regressions are shown excluding (solid lines) and including (dashed lines) SQ11. Error bars represent long-term external 2SD reproducibility.

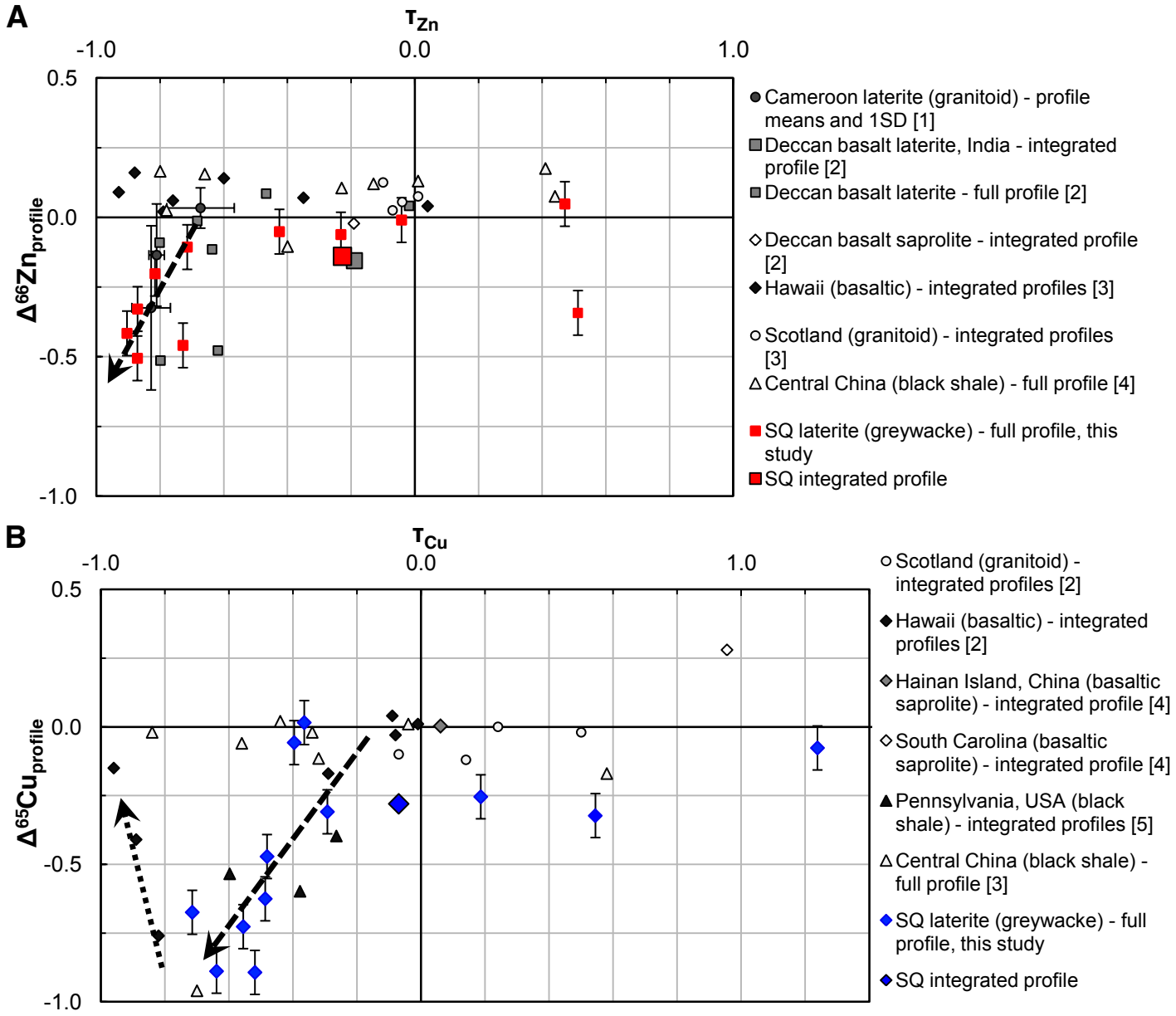

Figure 9. Integrated τ and integrated isotopic compositions for global soils **A**. Zn and **B**. Cu. Note, data are only included for studies where τ values are reported or can be calculated (Viers et al., 2007; Mathur et al., 2012; Liu et al., 2014; Lv et al., 2016; Vance et al., 2016). In order to include as much data as possible, but where an integrated τ-value cannot be calculated because horizon depths are not reported, either the full soil profile (for the central China black shale; Lv et al., 2016) or the mean and 1SD for each published profile (for the Cameroon laterite profiles; Viers et al., 2007) is shown. The SQ laterite dataset is shown as a full profile and as an integrated signature (larger symbol). Recently published full profile Zn isotope data is also included for the Bidar laterite, developed on Deccan basalt, for comparison (Zn only: Suhr et al., 2018). Literature data: [1] Viers et al. (2007), [2] Suhr et al. (2018) [3] Vance et al. (2016), [4] Lv et al. (2016), [5] Liu et al. (2014), [6] Mathur et al. (2012).